Mitochondrial dysfunction increases fatty acid β-oxidation and translates into impaired neuroblast maturation

Matteo Audano[1*], Silvia Pedretti[1*], Maurizio Crestani[1], Donatella Caruso[1], Emma De Fabiani[1#], Nico Mitro[1#]

[1]DiSFeB, Dipartimento di Scienze Farmacologiche e Biomolecolari, Università degli Studi di Milano, Via Balzaretti 9, 20133, Milan, Italy

* These authors equally contributed.

[#] Corresponding authors:
Nico Mitro
email: nico.mitro@unimi.it, phone: +390250318253
Emma De Fabiani
email: emmadefabiani@unimi.it, phone: +390250318329

ORCID ID of authors:
Matteo Audano: 0000-0003-2791-4526
Silvia Pedretti: 0000-0001-6404-6321
Maurizio Crestani: 0000-0001-9230-1078
Donatella Caruso: 0000-0003-2115-778X
Emma De Fabiani: 0000-0003-2406-1468
Nico Mitro: 0000-0002-5000-3619

Keywords: Energy metabolism; Mitochondria; Neuron maturation, Neuro2a cells.

Abstract

The metabolic transition from anaerobic glycolysis and fatty acid β-oxidation to glycolysis coupled to oxidative phosphorylation is a key process for the transition of quiescent neural stem cells to proliferative neural progenitor cells. However, a full characterization of the metabolic shift and the involvement of mitochondria occurring during the last step of neurogenesis, from neuroblasts to neurons maturation, is still elusive. Here, we describe a model of neuroblasts, Neuro2a cells, with impaired differentiation capacity due to mitochondrial dysfunction. Using a detailed biochemical characterization consisting of steady state metabolomics and metabolic flux analysis, we found increased fatty acid β-oxidation as peculiar feature of neuroblasts with altered mitochondria. The consequent metabolic switch favored neuroblast proliferation at the expense of neuron maturation.

Abbreviations

[U-$^{13}C_x$]	Uniformly labeled ^{13}Carbon, x = labeled carbon number
36B4	Ribosomal protein, large, P0
ADP	Adenosine diphosphate
AMP	Adenosine phosphate
ATP	Adenosine triphosphate
Atp5a1	ATP synthase, H^+ transporting, mitochondrial F1 complex, alpha subunit 1
AUC	Area under the curve
BCA	Bicinchoninic acid
BLT-1	Block of lipid transport 1
BSA	Bovine serum albumin
Carnitine-C0	DL-Carnitine
Carnitine-C10	Decanoyl-L-carnitine
Carnitine-C12	Dodecanoyl-L-carnitine
Carnitine-C14	Tetradecanoyl-L-carnitine
Carnitine-C16:0	Hexadecanoyl-L-carnitine
Carnitine-C16:1	Hexadecenoyl-L-carnitine
Carnitine-C18:0	Octadecanoyl-L-carnitine
Carnitine-C18:1	Octadecenoyl-L-carnitine
Carnitine-C2	Acetyl-L-carnitine
Carnitine-C3	Propionyl-L-carnitine
Carnitine-C4	Butyryl-L-carnitine
Carnitine-C5	Valeryl-L-carnitine
Carnitine-C6	Hexanoyl-L-carnitine
Carnitine-C8	Octanoyl-L-carnitine
Carnitine-C9	Nonayl-L-carnitine
CCCP	Carbonyl cyanide m-chlorophenyl hydrazone
CoA	Coenzyme A
Cpt1a	Carnitine palmitoyl-transferase
Cs	Citrate synthase
DMEM	Dulbecco's modified Eagle's medium
E4P	Erythrose-4-phosphate
EtBr	Ethidium bromide

ETC	Electron transport chain
F1,6BP	Fructose-1,6-bisphosphate
$FADH_2$	Flavin adenine dinucleotide reduced
FBS	Fetal bovine serum
FDR	False discovery rate
G6P/F6P	Glucose/Fructose-6-phosphate
GAP/DHAP	Glyceraldehyde-3-phosphate/Dihydroxyacetone phosphate
H2DCFDA	2′,7′-Dichlorodihydrofluorescein diacetate
HPLC	High-performance liquid chromatography
Hsp90	Heat-shock protein 90
HTS	High-throughput screening
Idh3	NAD^+-dependent isocitrate dehydrogenase 3
LC-MS/MS	Liquid chromatography tandem mass spectrometry
MID	Mass isotopomer distribution
MRM	Multiple reaction monitoring
mt-COI	Cytochrome C oxidase subunit 1
mtDNA	mitochondrial DNA
mt-ND1	Mitochondrially Encoded NADH:Ubiquinone Oxidoreductase Core Subunit 1
N2a	Neuro2a cells
NAA	N-acetylaspartate
NAD^+	nicotinamide adenine dinucleotide
NADH	nicotinamide adenine dinucleotide reduced
$NADP^+$	Nicotinamide adenine dinucleotide phosphate
NADPH	Nicotinamide adenine dinucleotide phosphate reduced
Ndufb8	NADH dehydrogenase [ubiquinone] 1 beta subcomplex subunit 8
NPCs	Neural progenitor cells
NSCs	Neural stem cells
OAA	Oxaloacetate
OCR	Oxygen consumption rate
Oligo	Oligomycin
Oxphos	Oxidative phosphorylation
PBS	Phosphate buffer saline
PEP	Phosphoenolpyruvate

PITC	Phenylisothiocyanate
Ribu/Xilu/Ribo5P	Ribulose/Xylulose/Ribose-5-phosphate
RIPA buffer	Radio immunoprecipitation assay buffer
ROS	Reactive oxygen species
RT	Room temperature
Sdhb	Succinate dehydrogenase subunit b
SDS-PAGE	Sodium dodecyl sulfate polyacrylamide gel electrophoresis
SR-B1	Scavenger receptor class B type 1
TBS	Tris buffered saline
TCA	tricarboxylic acid
Tfam	Transcription factor A mitochondria
TMPD	N,N,N′,N′-tetramethyl-p-phenylenediamine
Tubb3	Tubulin Beta 3 Class III
Tuj1	Neuron-specific class III beta-tubulin
Uqcrc2	Ubiquinol-Cytochrome C Reductase Core Protein 2

Introduction

Mitochondria are ubiquitous and multi-functional organelles involved in several cellular processes, such as energy production and synthesis of metabolites regulating vital functions. During the developmental process, cells change their metabolic states to support cellular differentiation [1,2]. Therefore, cells need a substantial amount of energy to cope with the newly established homeostasis that they have acquired during cellular differentiation. In other words, cells shift from glycolysis to oxidative phosphorylation (Oxphos), thus mitochondrial function and biogenesis are boosted during the cellular differentiation process [1,2]. Several lines of evidences demonstrate that interference with mitochondrial biogenesis during differentiation slows down or even blocks the differentiation process [1–3].

The neurogenic process – known as neurogenesis – in mammals is accomplished by neural stem cells (NSCs) at the prenatal phase and is maintained during postnatal stage, even though the presence of NSCs in adult brain is still matter of debate [4–6]. Mitochondria play key role in NSCs during development and adulthood to maintain proper neurological functions [7]. As mentioned above, NSCs, as well as other progenitor cells, during the generation of the neuronal lineage switch their metabolism from primarily anaerobic glycolysis and fatty acid catabolism to glycolysis that requires actively functional mitochondria [7]. In addition, glutamine metabolism is increased during of neuron differentiation [8]. Neuronal cell fate becomes more apparent at the neural progenitor cells (NPCs) stage. Neurons differentiated from NPCs undergo morphological changes via axonal and dendritic arborization, resulting in a change in cell polarity. Newborn neurons migrate to their destination and make connections with pre-existing neurons by forming synapses and integrating into an established neuronal circuit. In addition, during the transition from NSCs to NPCs, mitochondria change their shape from elongated to fragmented, a process required for cell cycle exit to support cellular differentiation [7–9]. Finally, NPCs give rise to committed neuroblasts, the last differentiation step before the mature neurons.

Several efforts have been done to disentangle the role of mitochondria and metabolism in quiescent and proliferative NSCs [10], or during the transition from NSCs to NPCs [7,9,11]. Nevertheless, little is currently known about metabolic changes and thus the role of mitochondria during the maturation phase from neuroblasts to neurons.

Here, we took advantage of a widely used model of neuroblasts, such as Neuro2a cells (N2a), with impaired differentiation capacity due to chemically induced mitochondrial dysfunction. Biochemical characterization of these cells revealed increased fatty acid β-oxidation as peculiar feature of neuroblasts with altered mitochondria, that favored neuroblast proliferation to the detriment of neuron maturation. Our data highlighted that proper mitochondrial activity and metabolism in

neuroblasts is necessary in the final transition to neurons, as it occurs in the preceding stages of neurogenesis.

Materials and methods

Cell lines

Neuro2a cells (ATCC, CCL-131) were maintained in growth medium (high-glucose DMEM) supplemented with 10% fetal bovine serum (FBS) (v/v) (Euroclone), 1% glutamine (v/v) (Thermo Fisher Scientific), 1% penicillin/streptomycin (v/v) (Thermo Fisher Scientific) and in 37°C, 5% CO2 and 90% humidified atmosphere. N2a were differentiated by growing cells to 50% of confluence and switching growth medium to differentiation medium (1% FBS (v/v), 1% glutamine (v/v), 1% penicillin/streptomycin (v/v). Neuro2a cells were treated for 30 days with ethidium bromide 100ng/ml. Complete media was supplemented with 400μM uridine (U3750, Sigma Aldrich) and 1mM pyruvate (11360070, Thermo Scientific).

Cell proliferation assay

N2a cells were seeded at a density of 5 x 10^4 per cm^2 in black 96-well plates and incubated in complete medium. 24, 48 and 72 hours later, cells were washed in PBS and exposed to 32μM of Hoechst (33258, Life Technologies) in DMEM for 45 minutes at 37° C in the dark. Cells were washed again in PBS and fluorescence (wavelength of 445nm) was revealed by using EnVision plate reader (2100, Perkin Elmer).

Cell viability assay

N2a cells were seeded at a density of 5 x 10^4 per cm^2 in black 96-well plates and incubated in complete medium. 24 and 48 hours later, cells were washed in PBS and exposed to 5mg/ml of 3-(4,5-dimethylthiazol-2-yl)-2,5-diphenyltetrazolium bromide (MTT) reagent in PBS for 30 minutes at 37° C. Cells were washed again in PBS, lysed in 100μl of DMSO and shacked for 5 min. Absorbance (wavelength of 590nm) was revealed by using EnVision plate reader (2100, Perkin Elmer).

ROS level quantification

N2a cells were seeded at a density of 5 x 10^4 per cm^2 in black 96-well plates and incubated in complete medium. 24 hours later, cells were washed in PBS and exposed to 10μM of H_2DCFDA (D399, Life Technologies) and 32μM of Hoechst (33258, Life Technologies) in DMEM for 45 minutes at 37° C in the dark. Cells were washed again in PBS and fluorescence (wavelength of 529nm for H_2DCFDA and 445nm for Hoechst, respectively) was revealed by using EnVision plate reader (2100, Perkin Elmer).

Neurite quantification

N2a were fixed in formalin for 10 minutes and then stained for 20 min with the following solution: 0.02% Coomassie brilliant blue R-250 (w/v) in methanol: acetic acid: water, 46.5:7:46.5 (v/v/v) [12]. Cells were then extensively rinsed in sterile water and images were acquired in brightfield. Cell number was quantified by ImageJ software while neurite number, neurite length and neurite contacts were quantified by NeuronJ software.

Mitochondrial DNA (mtDNA) quantity and relative transcription quantification

Total DNA and mtDNA were isolated using genomic DNA from tissues kit (Macherey-Nagel, 740952.250). Briefly, samples were scraped from dishes and spun at 2,000g for 3 min at RT. Cells were then resuspended in lysis buffer and DNA was isolated following manufacturer's instructions. Samples were eluted in 60µl of DNase and RNase free water and quantified by UV spectrophotometry (NanoDrop 1000 Spectrophotometer, Thermo Fisher Scientific). Mitochondrial DNA content was evaluated by assessing mt-ND1 and 36B4 content as mitochondrial and nuclear-encoded genes, respectively. mt-DNA transcription was evaluated by normalizing mitochondrially encoded RNA on mtDNA content. Primers and probes were obtained from Eurofins Genomics MWG-Operon and are available upon request.

Western blot

Protein relative quantification analyses were carried out by separating cell lysates on SDS-PAGE. Cells were rinsed in ice-cold PBS, centrifuged and resuspended in RIPA buffer without SDS. Protein concentration was measured using BCA method (EMP014500, Euroclone). Proper protein amount was then resuspended in 1:1 v/v SDS-sample buffer and loaded on SDS-PAGE. After gel run, proteins were transferred to a nitrocellulose membrane and blocked in 5% bovine serum albumin (BSA, A8022, Sigma Aldrich) for 1 hour at RT. Membranes were then incubated O/N at 4°C with primary antibodies, previously resuspended in 0,1% TBS-Tween20 and 3% BSA. After extensive washes, membranes were incubated with HRP-conjugated secondary antibodies for 1.5 hour at RT. After washing, membranes were finally incubated with ECL substrate for bands detection. Primary and secondary antibodies were diluted as follows: OXPHOS cocktail 1:2000 (Abcam, ab110413), Tuj1 (D71G9, Cell Signaling), Hsp90 1:1000 (Santa Cruz Biotech., sc-7947). Blots were quantified by ImageJ software.

Oxygen consumption measurements

Oxygen consumption rate (OCR) analysis on whole cells was performed by using a Clark type oxygen electrode (Hansatech, DW1 electrode chamber). N2a cells were rinsed in pre-warmed PBS (37°C) and suspended in coupled respiration buffer (2% free fatty acids-BSA, 1mM Na-pyruvate, 25 mM D-glucose, 40 ng/ml digitonin) or electron flow buffer (2% free fatty acids -BSA, 10mM Na-pyruvate, 2mM malate, 4µM carbonyl cyanide m-chlorophenyl hydrazine (CCCP), digitonin 40ng/ml). Samples were then transferred to the electrode chamber for the oxygen consumption rate measurement. After measuring basal respiration, uncoupled and maximal respiration were evaluated by adding 5µM oligomycin and 5µM CCCP, respectively. Complex I, II and IV activities were evaluated through the electron flow protocol. Once transferred into the chamber, CI activity was evaluated. After 5µM rotenone and 2.5mM succinate addition, we assessed complex II activity. We then added 50µM antimycin A and 12.5mM/0.5mM Ascorbate/N,N,N',N'-tetramethyl-p-phenylenediamine (TMPD) to measure complex IV activity. Samples values were normalized on total protein content.

Steady state metabolomics and metabolite flux analysis

Cells were grown in 6-well plates, harvested in ice-cold PBS and centrifuged at 2,000g for 3 min at 4°C. Pellets were then resuspended in 250µl methanol/acetonitrile 1:1 containing [U-$^{13}C_6$]-Glucose (Sigma Aldrich, 389374) and [U-$^{13}C_5$]-Glutamine 1ng/µl (Sigma Aldrich, 605166) as internal standards and spun at 20,000g for 5 min at 4°C. Supernatant were then passed through a regenerated cellulose filter, dried and resuspended in 100µl of MeOH for subsequent analysis. Amino acids quantification was performed through previous derivatization. Briefly, 50µl of 5% phenyl isothiocyanate (PITC) in 31.5% EtOH and 31.5% pyridine in water were added to 10µl of each sample. Mixtures were then incubated with PITC solution for 20 min at RT, dried under N_2 flow and suspended in 100µl of 5mM ammonium acetate in MeOH/H_2O 1:1. Metabolomic data were performed on an API-4000 triple quadrupole mass spectrometer (AB Sciex) coupled with a HPLC system (Agilent) and CTC PAL HTS autosampler (PAL System) and on SCIEX Triple Quad™ 3500 LC-MS/MS. The identity of all metabolites was confirmed using pure standards. Quantification of different metabolites was performed with a liquid chromatography/tandem mass spectrometry (LC-MS/MS) method using a C18 column (Biocrates) for amino acids, Pursuit XRs Ultra 2.8 Diphenyl (Varian) for acyl-carnitine and cyano-phase LUNA column (50mm x 4.6mm, 5µm; Phenomenex) for metabolites, respectively. Methanolic samples were analyzed by a 10 min and 3 min run in positive (amino acids and acyl-carnitine) and 5 min run in negative (all other metabolites) ion mode with a 35 multiple reaction monitoring (MRM) transition in positive ion mode and 30 MRM transition in

negative ion mode, respectively. The mobile phases for positive ion mode analysis (amino acids) were phase A: 0.2% formic acid in water and phase B: 0.2% formic acid in acetonitrile. The gradient was T_0 100%A, $T_{5.5min.}$ 5%A, T_{7min} 100%A with a flow rate of 500µl/min. The mobile phase for acyl-carnitine analysis was 0.1% formic acid in MeOH in isocratic condition with a flow rate of 300µl/min. The mobile phase for negative ion mode analysis (all other metabolites) was phase A: Water and B: 2 mM ammonium acetate in MeOH. The gradient was 90% B for all the analysis with a flow rate of 500µl/min. MultiQuant™ software (version 3.0.2) was used for data analysis and peak review of chromatograms. Metabolomic data were normalized by defining x_n^N (relative metabolite area) as:

$$x_n^N = \frac{Xn}{\sum_{n=a}^{z} n}$$

where x_n represents the peak areas of metabolite n for samples $a, b, \ldots, z$ and $\sum_{n=a}^{z} n$ represents the sum of peak areas of metabolite n for samples $a, b, \ldots, z$.

Relative metabolite area (x_n^N) was then divided by the sum of relative metabolite areas analyzed in each sample to obtain relative metabolite abundance (m), as:

$$m_a^N = \frac{x_n^N}{\sum_{a=1}^{n} a}$$

where $\sum_{a=1}^{n} a$ represents the sum of relative metabolite areas *1, 2, ..., n* for sample *a.* Internal standards were used to control instrument sensitivity.

For metabolic tracing analyses, N2a cells were exposed for 24 hours to [U-$^{13}C_6$]-Glucose 1mM or [U-$^{13}C_5$]-Glutamine 2mM or [U-$^{13}C_{16}$]-Palmitate 100µM (Sigma Aldrich, 605573). Metabolite isotopomers quantification was performed as described above after setting 139 new MRMs. Heatmap and principal component analysis (PCA) were obtained by interrogating MetaboAnalyst 4.0 webtool (https://www.metaboanalyst.ca/) [13].

Statistical analysis

Statistical analyses were performed with Student's *t*-test or two-way ANOVA followed by Sidak's multiple comparison test using GraphPad Prism (version 6.0) and MetaboAnalyst 4.0 [13] where indicated. Grubbs'test (https://www.graphpad.com/quickcalcs/Grubbs1.cfm) and principal component analyses (a feature of MetaboAnalyst 4.0 https://www.metaboanalyst.ca/)
were used to identify eventual outliers, however no outliers were detected. n (reported in each figure legends) represents number of independent cell culture preparations.

Results

Generation of a model of dysfunctional mitochondria in neuroblasts

In order to unravel the role of mitochondria and metabolism in Neuro2a (N2a) cell differentiation, we used a gene independent approach to alter mitochondrial function. Therefore, N2a cells were treated for 30 days with a low dose of ethidium bromide (EtBr, 100ng/ml). Surprisingly, undifferentiated EtBr treated N2a cells showed increased mitochondrial DNA (mtDNA) levels (Fig. 1a). Given the polycistronic nature of mitochondrial RNA, the analysis of a gene encoded by mitochondrial genome is indicative of mitochondrial RNA abundance. Therefore, we normalized mtND1 steady state mRNA with mtDNA levels as a proxy of mitochondrial genome transcription. As reported in Fig. 1a, data suggest that EtBr treatment, despite increasing mtDNA content, reduced its transcription. This result was further corroborated by decreased levels of mtDNA-encoded COI (a subunit of electron transport chain (ETC) complex IV), and nuclear encoded subunit Sdhb (a subunit of ETC complex II) and Ndub8 (a subunit of ETC complex I) (Fig. 1b). In line with these findings, basal, uncoupled and maximal uncoupled respiration were significantly reduced in N2a EtBr-treated cells, as well as complex I, II and IV activities (Fig. 1c and d), while total reactive oxygen species (ROS) levels were unchanged (Fig.1e).

We next decided to demonstrate that chemically-induced Oxphos deficiency impacts significantly the biology of N2a cells. Based on the observation that cells exhibiting defective Oxphos are less capable to grow in galactose rich medium [14], we evaluated cell viability in control and EtBr-treated cells in the presence of 4.5 g/L galactose. In line with the fact that, in the absence of glucose, the ability to use galactose as energy substrate relies on Oxphos-derived ATP, EtBr-treated cells showed reduced cell growth compared to wild type (Fig. 1f). Notably, cell proliferation in glucose-containing media was comparable between wild type and EtBr-treated cells, suggesting that glycolysis may compensate the Oxphos deficiency (Fig. 1g). Collectively, these findings showed that a low dose of EtBr treatment is sufficient to alter mitochondrial function and metabolism in N2a cells.

Phenotypic effects of Oxphos deficiency on N2a differentiation

To evaluate the effects of EtBr on N2a cell differentiation, we assessed cellular morphology and the expression of differentiation markers. From a morphological point of view, N2a wild type cells properly differentiated as evidenced by neurite network formation (Fig. 2a and Supplementary Fig. 1a) and cell cycle exit, sustained by reduced cell number compared to proliferating neuroblasts (Supplementary Fig. 1b). On the other hand, N2a EtBr-treated cells displayed reduced neurite number, length and contacts (Fig. 2a and b; Supplementary Fig. 1a). Furthermore, mRNA (*Tubb3*) and protein levels of Tuj1 were significantly decreased in EtBr-treated cells (Fig. 2c and d).

Basal, uncoupled and maximal uncoupled respiration and ETC complex activities in wild type and EtBr differentiated cells suggested that the differentiation impairment was due to Oxphos deficiency. As shown in fig. 2e, EtBr treated N2a still retained defects in oxygen consumption rates under basal conditions and also displayed a reduction of ETC complex I activity. ETC complex II and IV activities showed a trend to increase, probably to compensate the respiratory defects in complex I. These results were further sustained by Oxphos protein levels, indeed Ndufb8 (ETC complex I subunit) was reduced while Sdhb (ETC complex II subunit) and Atp5a1 (a subunit of ATPase complex) were increased (Fig 2f and g). Together these data demonstrated that EtBr treatment blunted N2a differentiation process as well as mitochondrial function.

Mitochondrial dysfunctional N2a neuroblasts show impaired metabolic profile

On the basis of the data previously reported and the tight relationship between mitochondria, metabolism and cell differentiation, we analyzed the intracellular metabolite levels. To capture early changes that may act as drivers of the observed phenotype, we conducted steady state metabolomics in undifferentiated wild type and Oxphos deficient N2a. Principal component analysis significantly discriminated the wild type cell population from that of N2a treated with EtBr (Supplementary Fig. 2). Steady state measurements indicated that among 58 metabolites detected, 18 were significantly changed (Fold change > 1.5; False Discovery Rate (FDR) < 0.1) in EtBr treated neuroblasts compared to wild type cells (Fig. 3a). Specifically, 9 metabolites such as arginine, aspartate, glutamine, glyceraldehyde-3-phosphate/dihydroxyacetone phosphate, phosphoenolpyruvate, pyruvate, ribulose/xylulose/ribose-5-phosphate, fumarate and malate were decreased in N2a EtBr treated cells (Fig 3b). On the other hand, 9 metabolites such as ADP, $NADP^+$, tryptophan, acetyl-L-carnitine (carnitine-C2), octanoyl-L-carnitine (carnitine-C8), tetradecanoyl-L-carnitine (carnitine-C14), hexadecanoyl-L-carnitine (carnitine-C16:0) and hexadecenoyl-L-carnitine (carnitine-C16:1) and octadecenoyl-L-carnitine (carnitine-C18:1) were increased in EtBr treated N2a undifferentiated cells compared to wild type (Fig. 3c). Moreover, carnitine-C16:0 + octadecanoyl-L-carnitine (carnitine-C18:0)/free carnitine (carnitine-C0) ratio, as measure of the activity of carnitine palmitoyl-transferase 1a (Cpt1a), was increased in EtBr N2a, as well as carnitine-C2/carnitine-C0 ratio, indicating higher β-oxidation of fatty acids (Supplementary Fig. 3a and b). Overall, these data suggest that neuroblasts with dysfunctional mitochondria exhibit impaired glycolysis and amino acid metabolism. The increased levels of several carnitines strongly suggest a preferential use of fatty acids.

Neuroblasts with dysfunctional mitochondria use fatty acids oxidation to sustain cell proliferation

To evaluate the dependence on extracellular lipids of both wild type and EtBr N2a cells, we used scavenger receptor, class B, type I (SR-BI) lipid transporter antagonist BLT-1 (block of lipid transport 1) and measured cell proliferation. As shown in Fig. 4a both wild type and EtBr cells showed decreased growth compared to vehicle-treated cells, suggesting that lipid uptake is requested to maintain the proliferation rate. Next, in order to discriminate if fatty acid contribution to cell proliferation is also mediated by their oxidation in mitochondria, we challenged cells with palmitate in the absence or presence of carnitine. The enzyme Ctp1a, localized on the outer mitochondrial membrane, leverages carnitine to transfer fatty acids into mitochondria, representing the rate limiting step of fatty acid oxidation. In the absence of carnitine, palmitate was uncapable to sustain cell survival (Fig. 4b), instead carnitine promoted fatty acid β-oxidation and sustained cell viability in EtBr-treated N2a cells (Fig. 4c). These data were further sustained by significantly reduced cell viability in EtBr-treated cells exposed to etomoxir, the chemical inhibitor of Cpt1a (Fig. 4d). Furthermore, EtBr-treated N2a cultured in presence of carnitine and palmitate showed increased ROS levels (Fig. 4e). This is probably due to the impaired Oxphos of EtBr-treated N2a that inefficiently cope with the overload of reducing cofactors (NADH and $FADH_2$) deriving from fatty acid oxidation.

Taken together, these data demonstrated that EtBr-treated N2a cells rewired their metabolism and showed greater dependence on palmitate oxidation compared to wild type cells to sustain cell proliferation.

Neuroblasts with dysfunctional mitochondria exhibit altered tricarboxylic acid (TCA) cycle and utilization of energy substrates

To gain more detailed insight into metabolism of EtBr-treated neuroblasts, we cultured cells in the presence of 1mM [U-$^{13}C_6$]glucose, 1mM [U-$^{13}C_5$]glutamine, or 100μM [U-$^{13}C_{16}$]palmitate for 24 hours and analyzed the labeling of TCA cycle intermediates in each condition. As shown in Fig. 5a, EtBr-treated N2a cells incorporated comparable amount of carbons from labeled glucose into M2 acetyl-CoA of wild type cells, suggesting a comparable rate of glucose oxidation through glycolysis. The incorporation of one molecule of labeled acetyl-CoA into citrate (first entry of glucose-derived carbons in the TCA cycle, carbons 1 and 2) was similar in both EtBr and wild type cells suggesting that citrate synthase (Cs) activity was not affected. In contrast, M2 citrate labeled in carbons 3 and 4, indicative of a single TCA cycle round was downregulated in EtBr treated cells (Fig. 5b). On the other hand, M4 citrate (carbons 1, 2, 3 and 4), originated by the incorporation of two molecules of M2 acetyl-CoA, was increased in EtBr treated cells (Fig. 5b). These data suggest that in Oxphos

deficient N2a Cs activity is not affected, while the defects may reside in other downstream reactions of the TCA cycle. This concept is further sustained considering the incorporation of [U-$^{13}C_6$]glucose-derived carbons in α-ketoglutarate (αKG), an intermediate formed downstream of citrate. Indeed, M2 αKG (labeled in 1 and 2 deriving from citrate M2 labeled in 1 and 2) and M2 αKG (labeled carbons 3 and 6 from multiple TCA cycles) were decreased in N2a treated with EtBr (Fig. 5c), as well as M3 αKG produced from M4 citrate after NAD^+-dependent isocitrate dehydrogenase 3 (Idh3) activity (Fig. 5c). Furthermore, no major differences were detected considering the incorporation of [U-$^{13}C_6$]glucose-derived carbons in oxaloacetate (OAA) (Fig. 5d). These data indicate a major defect in Idh3 activity.

Glutamine can be utilized in the mitochondria by oxidative metabolism and/or can be routed to the cytoplasmic reductive pathway. When undifferentiated wild type and EtBr-treated N2a cells where cultured in the presence of [U-$^{13}C_5$]glutamine, the levels of M2 acetyl-CoA were comparable between the two experimental conditions (Fig. 5e). Interestingly, the M2 citrate (labeled in carbons 1 and 2) produced by the glutamine reductive pathway and Cs activity was reduced in N2a treated with EtBr (Fig. 5f). Similarly, M2 citrate (labeled in positions 3 and 5) derived by glutamine reductive pathway and pyruvate carboxylase activity was significantly decreased in Oxphos deficient cells (Fig. 5f). Conversely, M5 citrate produced by reductive pathway (labeled in carbons 1, 2, 3, 5 and 6), as well as M4, M5 (labeled in positions 1, 2, 3, 4 and 5) and M6 citrate forms originated from glutamine oxidative metabolism were unchanged (Fig. 5f). These results are further substantiated by decreased levels of M2 (derived from citrate labeled in positions 1 and 2) and M3 (produced by citrate M4) αKG detected in N2a with dysfunctional mitochondria (Fig. 5g). Levels of M5 αKG were comparable between experimental groups, indicating that glutamine conversion to αKG is not affected by EtBr treatment (Fig 5g). In addition, M3 OAA levels, only ascribable to reductive glutamine metabolism, were blunted in N2a cells treated with EtBr (Fig. 5h). Altogether, the analysis of isotopomers from glutamine labeling suggests a major defect in the reductive pathway and further confirms impaired Idh3 activity.

Next, we investigated fatty acid utilization by means of [U-$^{13}C_{16}$]palmitate tracing. In this experimental setting, we found that the incorporation of [U-$^{13}C_{16}$]palmitate-derived carbons in M2 acetyl-CoA was increased in EtBr-treated N2a cells compared to wild type (Fig. 5i). Furthermore, M2 (labeled in carbons 3 and 4) and M4 citrate, as well as M2 (from citrate labeled in positions 1 and 2) and M3 αKG, generated from several rounds of the TCA cycle, were increased in N2a with dysfunctional mitochondria (Fig. 5j and 5k). Also, M2 OAA (derived from the first TCA round) showed a trend to increase, while M3 OAA (derived from multiple TCA rounds) was decreased compared to wild type control (Fig. 5l). These observations are consistent with the increased β-

oxidation as indicated by steady-state metabolomics and reduced TCA cycle flux as indicated tracing analyses.

To gain a complete overview on the fluxes of different metabolic substrates into TCA, we calculated the contribution of each labeled substrate to citrate abundance. As reported in Fig. 5m and based on the above described data, N2a EtBr-treated cells showed *i*) significantly less glutamine flux in the reductive pathway, *ii*) accumulation of glucose-derived carbons in citrate due to reduced Idh3 activity and *iii*) increased fatty acid oxidation. Collectively, these data demonstrated that neuroblasts with dysfunctional mitochondria shift their metabolism towards more fatty acid oxidation compared to wild type cells (Fig 5n).

As reported above, EtBr-treated cells proliferated to the same extent of N2a wild type (Fig. 1f). In addition, we showed that in contrast to wild type cells, N2a with defective mitochondrial function exhibited increased fatty acid oxidation and higher capacity to grow in the presence of palmitate (Fig 3 and 4). We next sought to ascertain the fate of fatty acid-derived carbons. Indeed, several TCA cycle intermediates are substrates for amino acid synthesis, that in turn are key molecules required for cell viability. Notably, we found increased incorporation of [U-$^{13}C_{16}$]palmitate-derived carbons into M2 aspartate (derived from M2 OAA labeled in 1 and 2, Fig. 5l), M2 glutamate and M2 proline (from M2 αKG labeled in 1 and 2, Fig. 5k) in EtBr-treated N2a (Fig. 6a). Instead, M2 glutamine (from M2 glutamate) was unchanged between groups (Fig. 6b), while M3 glutamine (from M3 glutamate, undetectable levels) was decreased in N2a treated with EtBr compared to wild type cells (Fig. 6c). Considering metabolic labeling with [U-$^{13}C_6$]glucose, our analyses revealed unchanged levels of M2 aspartate between the experimental conditions (Fig.6d), while M2 glutamate, M2 proline, M2 and M3 glutamine were decreased compared to wild type control (Fig.6e). Furthermore, we observed decreased M2 aspartate, unchanged levels of M4 aspartate (Fig.6f), reduced M2 and M3 glutamate, and unchanged levels of M5 glutamate originating from [U-$^{13}C_5$]glutamine (Fig.6g) in EtBr-treated N2a compared to wild type cells. Moreover, we found decreased levels of M2 proline (Fig.6h) and M5 glutamine from the same labeled substrate in N2a cells with dysfunctional mitochondria (Fig.6i). Finally, we observed increased glucose derived M2 alanine, produced by pyruvate transamination in the cytoplasm (Supplementary Fig.4a), and no changes in other non-essential amino acids labeling (Supplementary Fig. 4b, c and d). Taken together, these data corroborate the metabolic re-channeling of glucose and palmitate derived carbons in EtBr-treated N2a cells to maintain key amino acid biosynthesis required for cell proliferation (Fig.6j).

Discussion

Neurogenesis is a biological process beginning from neural stem cells to mature neuron formation. This process is necessary for the development of the nervous system to ensure proper cognitive functions, such as behavior, mood, memory [1,15,16], and brain plasticity [17–21].

During neuronal devolvement, cells experience metabolic shift from mainly anaerobic glycolysis and fatty acid oxidation to higher glucose oxidative and glutamine metabolism [1,2]. Neurons consumes a substantial amount of glucose and glutamine to accomplish intra and extracellular signaling, dendritic and axonal transport, to re-establish action potential, and recycling of neurotransmitters after depolarization [8]. In the last few years, also lipid metabolism has been shown to contribute to neurogenesis, indeed Knobloch and colleagues demonstrated that lipogenesis is critical for neural differentiation [22], while fatty acid oxidation is fundamental for the proliferation of neural stem/progenitor cell pool [9,10,23]. However, the biochemical mechanisms leading to decreased fatty acid oxidation during neural differentiation are not yet fully understood. The main hypothesis is that fatty acids β-oxidation yields a great amount of reducing cofactors (NADH and $FADH_2$) and acetyl-CoA, whose carbons are diverted to a limited number of anaplerotic reactions in neuron precursors. Instead, glucose and glutamine metabolism are more flexible and dynamic. Specifically, glucose can be oxidized in the glycolysis or diverted to pentose phosphate pathway. Then, at the end of the glycolysis, pyruvate replenishes: *i*) cytoplasmic lactate for NAD^+ recycling; *ii*) TCA cycle; *iii*) lipid synthesis and *iv*) cytoplasmic alanine levels and aspartate in both mitochondria and cytosol. Glutamine is converted to glutamate by cytosolic glutaminase-catalyzed deamination. In turn, glutamate is converted to αKG in the cytoplasm by glutamic-oxaloacetic transaminase 1 (Got1) to feed glutamine reductive pathway for lipid and aspartate synthesis. Got2 catalyzes the same transamination in the mitochondria to fuel TCA cycle (oxidative pathway) [8,24,25]. Aspartate, glutamine and glutamate directly sustain cell proliferation, being a source of nitrogen and carbon for nucleotide biosynthesis, but also cell differentiation, being important precursors for microtubule and synapse formation, as well as neurotransmitter biosynthesis [26,27]. Recent findings also prove that proper cell nutrients catabolism through TCA cycle and ETC are instrumental to sustain aspartate production, and hence cell growth [28–32]. Nonetheless, aspartate together with acetyl-CoA forms N-acetylaspartate (NAA). NAA is fundamental for axon formation and mechanical support by functioning as acetyl groups donor to oligodendrocytes for lipid and myelin synthesis [33]. Hence, being pleiotropic metabolic alternatives, glucose and glutamine are preferred by mature neurons to support their metabolic requirements.

To sustain the metabolic rewiring during neuron maturation, mitochondria meet cellular demand by changing their dynamics and shape, thus triggering a bidirectional transcriptional program

that suppresses self-renewal, promotes differentiation, and leads to greater mitochondrial functionality during neurogenesis [34]. As a proof of this notion, perturbation of mitochondrial function in quiescent radial glia-like neural stem cells due to depletion of mitochondrial transcription factor A (Tfam) reproduces multiple hallmarks of aging in hippocampal neurogenesis [35]. In addition, other evidences elucidated the metabolic changes between quiescent and proliferative NSCs [10], or in the transition from NSCs to NPCs [7,9,11]. On the other hand, to date only few reports have addressed the role of mitochondria during the maturation process from neuroblasts to neurons [36–41], thus a detailed metabolic characterization of this transition is still incomplete.

Here, we develop a model of N2a cells with dysfunctional mitochondria to investigate the contribution of mitochondria and energy metabolism to the maturation from neuroblast to neuron. Specifically, cells were treated with EtBr to interfere with mtDNA biology in a gene-independent fashion. Indeed, EtBr-treated N2a cells show increased mtDNA amount but reduced mtDNA transcription, leading to impaired Oxphos function and efficiency compared to wild type N2a. Notably, EtBr-treated N2a show altered differentiation compared to wild type control due to less and shorter neurites, all of which result in a compromised cellular network formation. Conversely, the growth rate of Oxphos deficient N2a neuroblasts is unaffected, suggesting the strong ability of these cells to rewire their metabolism to sustain cell proliferation at the expense of differentiation.

Based on these findings, we focused our attention on the metabolic adaptation of EtBr-treated cells at neuroblast stage. Combining cell growth analyses, steady state metabolomics and metabolic flux analyses, we uncover the biochemical mechanisms underlying cell proliferation and differentiation of neuroblasts with Oxphos deficiency, highlighting the robust relationship between mitochondrial function, metabolic profile and cell development. Steady state metabolomics reveals increased levels of several acylcarnitines, reduced levels of glutamine, glutamate, aspartate and glycolysis intermediates in dysfunctional mitochondria N2a neuroblasts. Beyond this, flux analysis reveals: *i*) decreased TCA cycle flux, *ii*) lower incorporation of glucose and glutamine-derived carbons into amino acids from anaplerotic reactions, *iii*) increased abundance of palmitate-derived carbons into amino acids to replenish anaplerotic reactions, and *iv*) increased transamination of glucose-derived pyruvate into alanine, all of which indicate a reduced activity of Idh3. Consistently with reduced TCA cycle and ETC activity, we also observe increased ROS levels in Oxphos deficient cells only when forced to use β-oxidation by the exposure to palmitate and carnitine.

Altogether, our data demonstrate that during maturation from neuroblast to neuron, mitochondrial function and energy metabolism are not merely settled by nuclear transcription, instead they are interconnected and active players in the differentiation process. Moreover, we proved that

fatty acid β-oxidation is a biochemical brake of cell cycle exit, a key process required for neuroblasts maturation to neurons (Fig.7).

Figure legends

Fig. 1 Neuroblast N2a model of dysfunctional mitochondrial. **a** Relative mtDNA amount and mtDNA transcription levels (***p*<0.01; Student's *t*-test vs Wild type, n = 5). **b** Western blot of Oxphos subunits Uqcrc2, mt-COI, Sdhb and Ndufb8 and Hsp90 as loading control. **c** Basal, uncoupled and maximal uncoupled respiration and **d** complex I, II and IV activities (**p*<0.05; ***p*<0.01; ****p*<0.001; Student's *t*-test vs Wild type, n = 5). **e** Relative ROS levels (n = 8). **f** Cell proliferation based on relative DAPI intensity (to day 0) of N2a cells grown in 4.5g/L galactose, 2mM glutamine and 10% FBS (Area Under Curve (AUC), ****p*<0.001; Student's *t*-test vs Wild type, n = 8). Dashed line represents Wild type and EtBr cells grown in complete media. **g** Proliferation rate of N2a neuroblasts (n = 6). Black bars/lines = Wild type N2a; red bars/lines = EtBr-treated N2a. Data are expressed as mean ± SD.

Fig. 2 EtBr treatment affects N2a differentiation. **a** Representative brightfield images of 3 days differentiated wild type and EtBr-treated N2a after fixation and blue Coomassie staining (scale bar = 50µm). **b** Neurite number, length and contacts quantification (*p<0.05; **p<0.01; ***p<0.001; Student's t-test vs Wild type, n = 5). **c** *Tubb3* mRNA expression levels (*p<0.05; Student's t-test vs Wild type, n = 4). **d** Tuj1 western blot and relative quantification. Hsp90 represent loading control (*p<0.05; Student's t-test vs Wild type, n = 3). Black bars = Wild type N2a; red bars = EtBr-treated N2a. **e** Basal, uncoupled and maximal uncoupled respiration, and complex I, II and IV activities after 3 days of differentiation (*p<0.05; **p<0.01; ***p<0.001; Student's t-test vs Wild type, n = 3). **f** Representative western blot of Oxphos subunits Atp5a1, Uqcrc2, mt-COI, Sdhb and Ndufb8 and Hsp90 as loading control. **g** Western blot (**f**) quantification (*p<0.05; Student's t-test vs Wild type, n = 3). Data are expressed as mean ± SD.

Fig. 3 Steady-state metabolomic analysis of wild type and dysfunctional mitochondria neuroblasts. **a** *Z*-score-based heatmap and dendrogram of 58 detected metabolites. **b** Box plots of significantly decreased and **c** increased metabolites.
Gray boxes = Wild type N2a; Red boxes = EtBr-treated N2a. Data are expressed as mean ± SD. (False Discovery Rate (FDR) < 0.1, Fold Change > 1.5; *p<0.05; **p<0.01; ***p<0.001; Student's t-test vs Wild type, n = 4).

Fig. 4 Fatty acid β-oxidation favors EtBr-treated cells proliferation. **a** Proliferation rate of Wild type and EtBr neuroblasts treated with vehicle or Block of Lipid Transport-1 (BLT-1) 5µM for 48 hours (**p<0.01; ***p<0.001; two-way ANOVA followed by Sidak's multiple comparison test, n = 8). **b**

Relative cell viability (to Wild type with FBS) of Wild type and EtBr neuroblasts treated with palmitate at the indicated concentrations for 48 hours in the absence and **c** presence of 1mM carnitine (**p<0.01; ***p<0.001; Student's t-test vs Wild type, n = 8). **d** Relative ROS levels of N2a neuroblasts grown with 1mM carnitine and 100µM palmitate for 24 hours (***p<0.001; Student's t-test vs Wild type, n = 8). **e** Relative cell viability (to Wild type with vehicle) of Wild type and EtBr neuroblasts treated with vehicle or 100µM etomoxir for 24 hours (**p<0.01; Student's t-test vs Wild type, n = 8). Black bars/lines = Wild type N2a; red bars/lines = EtBr-treated N2a; purple line = BLT-1 treatment. Data are expressed as mean ± SD.

Fig. 5 Metabolic flux analysis indicate increased palmitate-derived carbons contribution to TCA cycle intermediates. **a** Mass isotopomer distribution (MID) of [U-$^{13}C_6$]-Glucose derived acetyl-CoA, **b** citrate, **c** α-ketoglutarate and **d** oxaloacetate (*p<0.05; **p<0.01; ***p<0.001; Student's t-test vs Wild type, n = 6). **e** MID of [U-$^{13}C_5$]-Glutamine derived acetyl-CoA, **f** citrate, **g** α-ketoglutarate and **h** oxaloacetate (*R* indicates metabolites originating from glutamine reductive pathway; *p<0.05; **p<0.01; ***p<0.001; Student's t-test vs Wild type, n = 6). **i** MID of [U-$^{13}C_{16}$]-Palmitate derived acetyl-CoA, **j** citrate, **k** α-ketoglutarate and **l** oxaloacetate (*p<0.05; **p<0.01; ***p<0.001; Student's t-test vs Wild type, n = 6). **m** Carbon contribution of different labeled substrates to citrate in Wild type and EtBr-treated neuroblasts (*p<0.05; **p<0.01; ***p<0.001; Student's t-test vs Wild type, n = 6). **n** Schematic representation of metabolic pathways obtained by flux analyses in Wild type and EtBr-treated neuroblasts. Black bars = Wild type N2a; red, green, blue bars = EtBr-treated N2a with [U-$^{13}C_6$]-Glucose, [U-$^{13}C_5$]-Glutamine and [U-$^{13}C_{16}$]-Palmitate, respectively; Black circles under bars represent ^{13}C labeled carbons; Data are expressed as mean ± SD. Carbon positions are schematically represented in each panel.

Fig. 6 Palmitate derived carbons flow into aspartate, glutamate and proline. **a** [U-$^{13}C_{16}$]-Palmitate derived M2 aspartate, glutamate, proline, **b** glutamine and **c** M3 glutamine levels (*p<0.05; **p<0.01; ***p<0.001; Student's t-test vs Wild type, n = 6). **d** [U-$^{13}C_6$]-Glucose derived M2 aspartate, **e** glutamate, proline, glutamine and M3 glutamine levels (**p<0.01; ***p<0.001; Student's t-test vs Wild type, n = 6). **f** [U-$^{13}C_5$]-Glutamine derived M2 and M4 aspartate, **g** M2, M3 and M5 glutamate, **h** M2 proline, **i** and M5 glutamine levels (*R* indicates metabolites originating from glutamine reductive pathway; *p<0.05; **p<0.01; ***p<0.001; Student's t-test vs Wild type, n = 6). **j** Schematic representation of labeled amino acids obtained by flux analyses in Wild type and EtBr-treated neuroblasts. Black bars = Wild type N2a; red, green, blue bars = EtBr-treated N2a with [U-$^{13}C_6$]-

Glucose, [U-$^{13}C_5$]-Glutamine and [U-$^{13}C_{16}$]-Palmitate, respectively; Data are expressed as mean ± SD.

Fig. 7 Schematic representation of the putative biochemical mechanism underlying neuroblast to neuron maturation in wild type and dysfunctional mitochondria N2a cells. Chemically induced mitochondrial impairment leads to altered metabolic profile, that by promoting fatty acid β-oxidation and pyruvate to alanine transamination sustain cell proliferation to the detriment of complete neuron maturation.

Supplementary Figure legends

Supplementary Fig. 1 EtBr treatment decreases neurite formation in N2a differentiated cells. **a** Representative brightfield images of 3 days differentiated wild type and EtBr-treated N2a after fixation and blue Coomassie staining (scale bar = 50μm). **b** Cell proliferation based on DAPI intensity of Wild type neuroblasts and 72h differentiated N2a (***p<0.001; Student's t-test vs Proliferating Wild type cells, n = 8). Black bar = Proliferating Wild type N2a; orange bar = Differentiated Wild type N2a. Data are expressed as mean ± SD.

Supplementary Fig. 2 EtBr treatment change metabolic profile of N2a neuroblasts. Principal Component Analysis (PCA) performed on targeted steady state metabolomics by MetaboAnalyst webtool.
Red circles = Wild type N2a; Green circles = EtBr-treated N2a. Red and green areas represent 95% confidence regions.

Supplementary Fig. 3 Carnitine ratios are increased after EtBr treatment. **a** Acetyl-L-carnitine (C2)/free carnitine (C0) ratio to indicate to measure β-oxidation of fatty acids. **b** Hexadecanoyl-L-carnitine (C16:0) + Octadecanoyl-L-carnitine (C18:0)/free carnitine (C0) ratio as measure of the activity of Cpt1a, the rate-limiting step in the uptake of fatty acids into mitochondria. Gray boxes = Wild type N2a; Red boxes = EtBr-treated N2a. Data are expressed as mean ± SD. (False Discovery Rate (FDR) < 0.1, Fold Change > 1.5; **p<0.01; Student's t-test vs Wild type, n = 4).

Supplementary Fig. 4 Glucose carbons converge to alanine. **a** [U-$^{13}C_6$]-Glucose derived M2 alanine (*p<0.05; Student's t-test vs Wild type, n = 6), **b** serine, arginine and glycine. **c** [U-$^{13}C_5$]-Glutamine derived M2 arginine and glycine. **d** [U-$^{13}C_{16}$]-Palmitate derived M2 arginine and glycine. Black bars

= Wild type N2a; red, green, blue bars = EtBr-treated N2a with [U-$^{13}C_6$]-Glucose, [U-$^{13}C_5$]-Glutamine and [U-$^{13}C_{16}$]-Palmitate, respectively; Data are expressed as mean ± SD.

Acknowledgments and conflict of interest disclosure

We thank F. Giavarini for his valuable help with HPLC and mass spectrometry. We are in debt with Ms. E. Desiderio Pinto and Dr. M. Marchesi for administrative assistance.

This work is supported by The Giovanni Armenise Harvard-Foundation Career Development Grant, Cariplo Foundation (grant number 2014-0991), intramural transition grant from Università degli Studi di Milano and MIUR Progetto Eccellenza. The authors declare no conflict of interest.

References

1 Teslaa T & Teitell MA (2015) Pluripotent stem cell energy metabolism: an update. *EMBO J.* **34**, 138–53.

2 Zhang H, Menzies KJ & Auwerx J (2018) The role of mitochondria in stem cell fate and aging. *Development* **145**, dev143420.

3 Xu X, Duan S, Yi F, Ocampo A, Liu GH & Izpisua Belmonte JC (2013) Mitochondrial regulation in pluripotent stem cells. *Cell Metab* **18**, 325–332.

4 Sorrells SF, Paredes MF, Cebrian-Silla A, Sandoval K, Qi D, Kelley KW, James D, Mayer S, Chang J, Auguste KI, Chang EF, Gutierrez AJ, Kriegstein AR, Mathern GW, Oldham MC, Huang EJ, Garcia-Verdugo JM, Yang Z & Alvarez-Buylla A (2018) Human hippocampal neurogenesis drops sharply in children to undetectable levels in adults. *Nature* **555**, 377–381.

5 Boldrini M, Fulmore CA, Tartt AN, Simeon LR, Pavlova I, Poposka V, Rosoklija GB, Stankov A, Arango V, Dwork AJ, Hen R & Mann JJ (2018) Human Hippocampal Neurogenesis Persists throughout Aging. *Cell Stem Cell* **22**, 589-599.e5.

6 Kempermann G, Gage FH, Aigner L, Song H, Curtis MA, Thuret S, Kuhn HG, Jessberger S, Frankland PW, Cameron HA, Gould E, Hen R, Abrous DN, Toni N, Schinder AF, Zhao X, Lucassen PJ & Frisén J (2018) Human Adult Neurogenesis: Evidence and Remaining Questions. *Cell Stem Cell* **23**, 25–30.

7 Khacho M, Harris R & Slack RS (2019) Mitochondria as central regulators of neural stem cell fate and cognitive function. *Nat. Rev. Neurosci.* **20**, 34–48.

8 Agostini M, Romeo F, Inoue S, Niklison-Chirou M V, Elia AJ, Dinsdale D, Morone N, Knight RA, Mak TW & Melino G (2016) Metabolic reprogramming during neuronal differentiation. *Cell Death Differ.* **23**, 1502–1514.

9 Beckervordersandforth R (2017) Mitochondrial Metabolism-Mediated Regulation of Adult Neurogenesis. *Brain Plast. (Amsterdam, Netherlands)* **3**, 73–87.

10 Knobloch M, Pilz G-A, Ghesquière B, Kovacs WJ, Wegleiter T, Moore DL, Hruzova M, Zamboni N, Carmeliet P & Jessberger S (2017) A Fatty Acid Oxidation-Dependent Metabolic Shift Regulates Adult Neural Stem Cell Activity. *Cell Rep.* **20**, 2144–2155.

11 Zheng X, Boyer L, Jin M, Mertens J, Kim Y, Ma L, Ma L, Hamm M, Gage FH & Hunter T (2016) Metabolic reprogramming during neuronal differentiation from aerobic glycolysis to neuronal oxidative phosphorylation. *Elife* **5**.

12 Mochizuki Y & Furukawa K (1987) Application of Coomassie brilliant blue staining to cultured hepatocytes. *Cell Biol. Int. Rep.*

13 Chong J, Soufan O, Li C, Caraus I, Li S, Bourque G, Wishart DS & Xia J (2018) MetaboAnalyst

4.0: Towards more transparent and integrative metabolomics analysis. *Nucleic Acids Res.*

14 Arroyo JD, Jourdain AA, Calvo SE, Ballarano CA, Doench JG, Root DE & Mootha VK (2016) A Genome-wide CRISPR Death Screen Identifies Genes Essential for Oxidative Phosphorylation. *Cell Metab.* **24**, 875–885.

15 Anacker C & Hen R (2017) Adult hippocampal neurogenesis and cognitive flexibility — linking memory and mood. *Nat. Rev. Neurosci.* **18**, 335.

16 Lazarov O & Hollands C (2016) Hippocampal neurogenesis: Learning to remember. *Prog. Neurobiol.* **138**–**140**, 1–18.

17 Bragado Alonso S, Reinert JK, Marichal N, Massalini S, Berninger B, Kuner T & Calegari F (2019) An increase in neural stem cells and olfactory bulb adult neurogenesis improves discrimination of highly similar odorants. *EMBO J.* **38**.

18 Silva-Vargas V, Crouch EE & Doetsch F (2013) Adult neural stem cells and their niche: a dynamic duo during homeostasis, regeneration, and aging. *Curr. Opin. Neurobiol.* **23**, 935–942.

19 Sailor KA, Schinder AF & Lledo P-M (2017) Adult neurogenesis beyond the niche: its potential for driving brain plasticity. *Curr. Opin. Neurobiol.* **42**, 111–117.

20 Lim DA & Alvarez-Buylla A (2014) Adult neural stem cells stake their ground. *Trends Neurosci.* **37**, 563–571.

21 Lepousez G, Nissant A & Lledo P-M (2015) Adult Neurogenesis and the Future of the Rejuvenating Brain Circuits. *Neuron* **86**, 387–401.

22 Knobloch M, Braun SMG, Zurkirchen L, von Schoultz C, Zamboni N, Araúzo-Bravo MJ, Kovacs WJ, Karalay Ö, Suter U, Machado RAC, Roccio M, Lutolf MP, Semenkovich CF & Jessberger S (2012) Metabolic control of adult neural stem cell activity by Fasn-dependent lipogenesis. *Nature* **493**, 226–230.

23 Knobloch M & Jessberger S (2017) Metabolism and neurogenesis. *Curr. Opin. Neurobiol.* **42**, 45–52.

24 Sonnewald U & McKenna M (2002) Metabolic compartmentation in cortical synaptosomes: influence of glucose and preferential incorporation of endogenous glutamate into GABA. *Neurochem. Res.* **27**, 43–50.

25 Erecińska M, Zaleska MM, Nissim I, Nelson D, Dagani F & Yudkoff M (1988) Glucose and synaptosomal glutamate metabolism: studies with [15N]glutamate. *J. Neurochem.* **51**, 892–902.

26 Peñalver A, Campos-Sandoval JA, Blanco E, Cardona C, Castilla L, Martín-Rufián M, Estivill-Torrús G, Sánchez-Varo R, Alonso FJ, Pérez-Hernández M, Colado MI, Gutiérrez A, de

Fonseca FR & Márquez J (2017) Glutaminase and MMP-9 Downregulation in Cortex and Hippocampus of LPA1 Receptor Null Mice Correlate with Altered Dendritic Spine Plasticity. *Front. Mol. Neurosci.* **10**, 278.

27 Erickson JD (2017) Functional identification of activity-regulated, high-affinity glutamine transport in hippocampal neurons inhibited by riluzole. *J. Neurochem.* **142**, 29–40.

28 Sullivan LB, Gui DY, Hosios AM, Bush LN, Freinkman E & Vander Heiden MG (2015) Supporting Aspartate Biosynthesis Is an Essential Function of Respiration in Proliferating Cells. *Cell* **162**, 552–63.

29 DeBerardinis RJ, Mancuso A, Daikhin E, Nissim I, Yudkoff M, Wehrli S & Thompson CB (2007) Beyond aerobic glycolysis: transformed cells can engage in glutamine metabolism that exceeds the requirement for protein and nucleotide synthesis. *Proc. Natl. Acad. Sci. U. S. A.* **104**, 19345–50.

30 Birsoy K, Wang T, Chen WW, Freinkman E, Abu-Remaileh M & Sabatini DM (2015) An Essential Role of the Mitochondrial Electron Transport Chain in Cell Proliferation Is to Enable Aspartate Synthesis. *Cell* **162**, 540–51.

31 Desler C, Lykke A & Rasmussen LJ (2010) The Effect of Mitochondrial Dysfunction on Cytosolic Nucleotide Metabolism. *J. Nucleic Acids* **2010**, 1–9.

32 Meléndez-Rodríguez F, Urrutia AA, Lorendeau D, Rinaldi G, Roche O, Böğürcü-Seidel N, Ortega Muelas M, Mesa-Ciller C, Turiel G, Bouthelier A, Hernansanz-Agustín P, Elorza A, Escasany E, Li QOY, Torres-Capelli M, Tello D, Fuertes E, Fraga E, Martínez-Ruiz A, Pérez B, Giménez-Bachs JM, Salinas-Sánchez AS, Acker T, Sánchez Prieto R, Fendt S-M, De Bock K & Aragonés J (2019) HIF1α Suppresses Tumor Cell Proliferation through Inhibition of Aspartate Biosynthesis. *Cell Rep.* **26**, 2257-2265.e4.

33 Moffett JR, Arun P, Ariyannur PS & Namboodiri AMA (2013) N-Acetylaspartate reductions in brain injury: impact on post-injury neuroenergetics, lipid synthesis, and protein acetylation. *Front. Neuroenergetics* **5**, 11.

34 Khacho M, Clark A, Svoboda DS, Azzi J, MacLaurin JG, Meghaizel C, Sesaki H, Lagace DC, Germain M, Harper ME, Park DS & Slack RS (2016) Mitochondrial Dynamics Impacts Stem Cell Identity and Fate Decisions by Regulating a Nuclear Transcriptional Program. *Cell Stem Cell* **19**, 232–247.

35 Beckervordersandforth R, Ebert B, Schäffner I, Moss J, Fiebig C, Shin J, Moore DL, Ghosh L, Trinchero MF, Stockburger C, Friedland K, Steib K, von Wittgenstein J, Keiner S, Redecker C, Hölter SM, Xiang W, Wurst W, Jagasia R, Schinder AF, Ming G, Toni N, Jessberger S, Song H & Lie DC (2017) Role of Mitochondrial Metabolism in the Control of Early Lineage

Progression and Aging Phenotypes in Adult Hippocampal Neurogenesis. *Neuron* **93**, 560-573.e6.

36 Vayssière J-L, Cordeau-Lossouarn L, Larcher JC, Basseville M, Gros F & Croizat B (1992) Participation of the mitochondrial genome in the differentiation of neuroblastoma cells. *Vitr. Cell. Dev. Biol. - Anim.* **28**, 763–772.

37 Agnihotri SK, Shen R, Li J, Gao X & Büeler H (2017) Loss of PINK1 leads to metabolic deficits in adult neural stem cells and impedes differentiation of newborn neurons in the mouse hippocampus. *FASEB J.* **31**, 2839–2853.

38 Kinoshita K, Ura H, Akagi T, Usuda M, Koide H & Yokota T (2006) GABPalpha regulates Oct-3/4 expression in mouse embryonic stem cells. *Biochem Biophys Res Commun* **353**, 686–691.

39 Keil U, Scherping I, Hauptmann S, Schuessel K, Eckert A & Müller WE (2006) Piracetam improves mitochondrial dysfunction following oxidative stress. *Br. J. Pharmacol.* **147**, 199–208.

40 Consalvi S, Saccone V, Giordani L, Minetti G, Mozzetta C & Puri PL (2011) Histone deacetylase inhibitors in the treatment of muscular dystrophies: epigenetic drugs for genetic diseases. *Mol Med* **17**, 457–465.

41 Puri R (2017) Protecting Mitochondrial Health: A Unifying Mechanism in Adult Neurogenesis. *J. Neurosci.* **37**, 6603–6605.

Figure 1

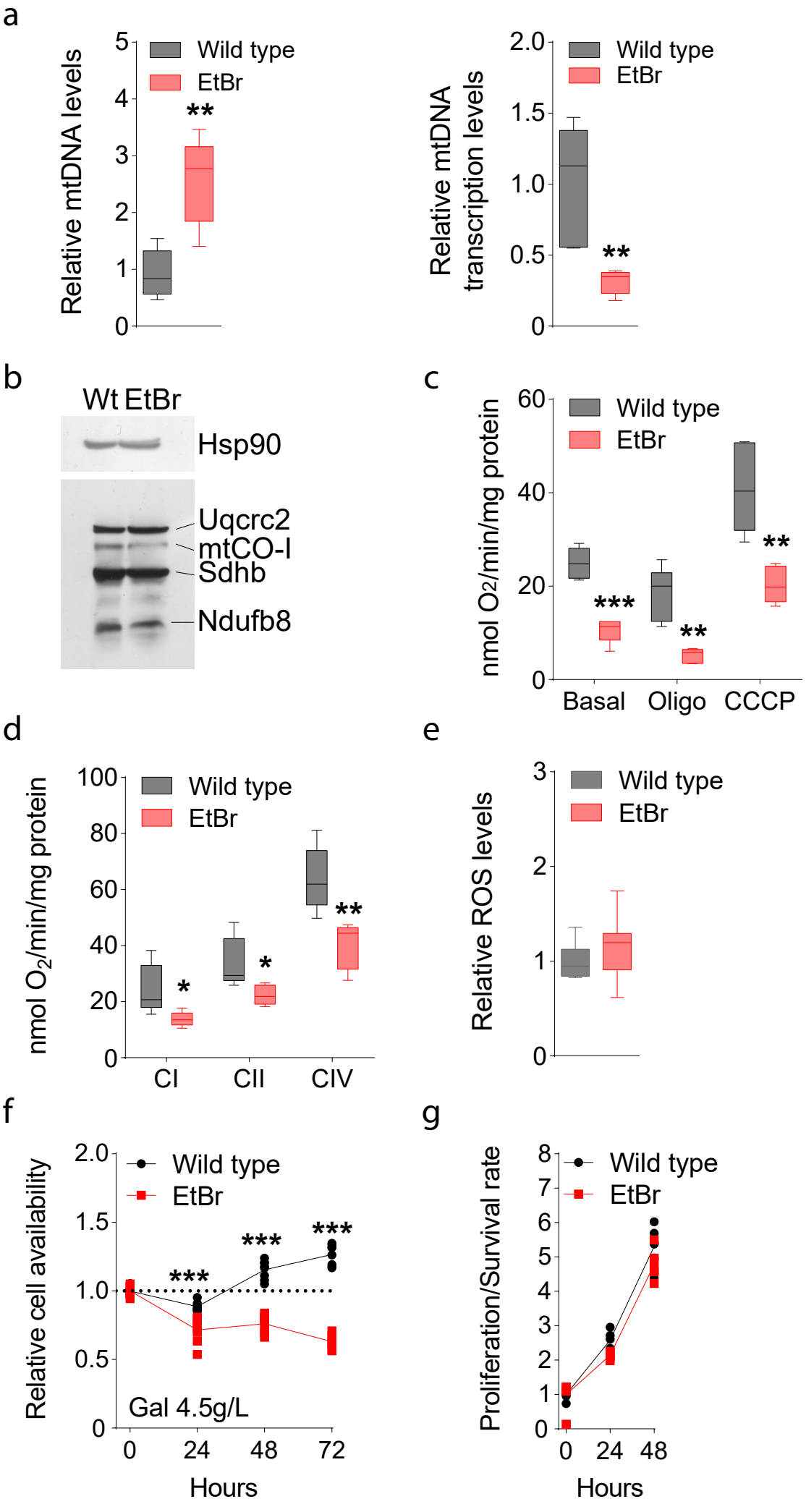
a
Relative mtDNA levels
Wild type
EtBr
**
Relative mtDNA transcription levels
b
Wt EtBr
Hsp90
Uqcrc2
mtCO-I
Sdhb
Ndufb8
c
nmol O2/min/mg protein
***
**
Basal
Oligo
CCCP
d
nmol O2/min/mg protein
*
CI
CII
CIV
e
Relative ROS levels
f
Relative cell availability
Gal 4.5g/L
Hours
g
Proliferation/Survival rate
Hours

Figure 2

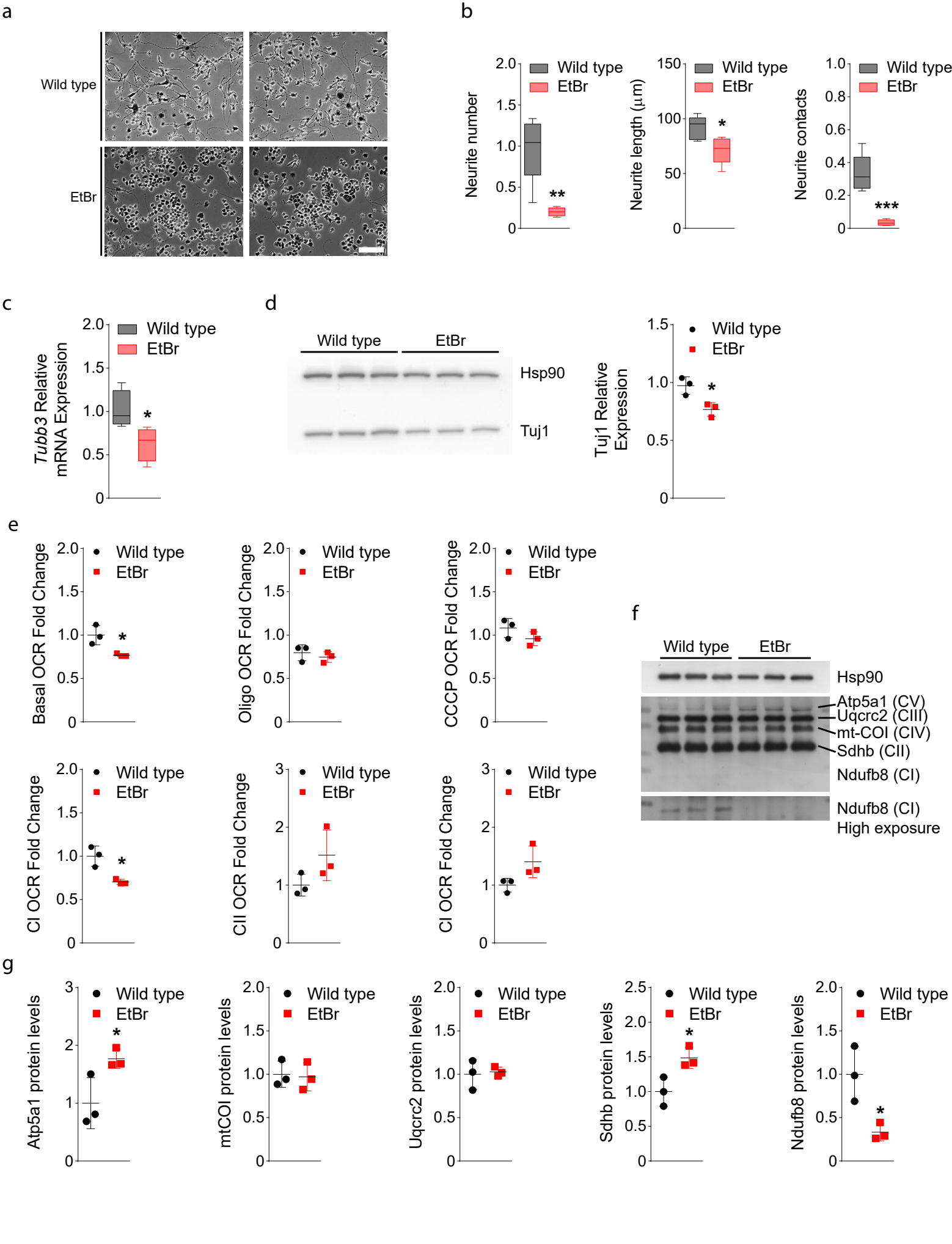
a
Wild type
EtBr
b
Neurite number
Neurite length (μm)
Neurite contacts
Wild type
EtBr
c
Tubb3 Relative mRNA Expression
d
Wild type
EtBr
Hsp90
Tuj1
Tuj1 Relative Expression
e
Basal OCR Fold Change
Oligo OCR Fold Change
CCCP OCR Fold Change
CI OCR Fold Change
CII OCR Fold Change
CI OCR Fold Change
f
Hsp90
Atp5a1 (CV)
Uqcrc2 (CIII)
mt-COI (CIV)
Sdhb (CII)
Ndufb8 (CI)
Ndufb8 (CI)
High exposure
g
Atp5a1 protein levels
mtCOI protein levels
Uqcrc2 protein levels
Sdhb protein levels
Ndufb8 protein levels

Figure 3

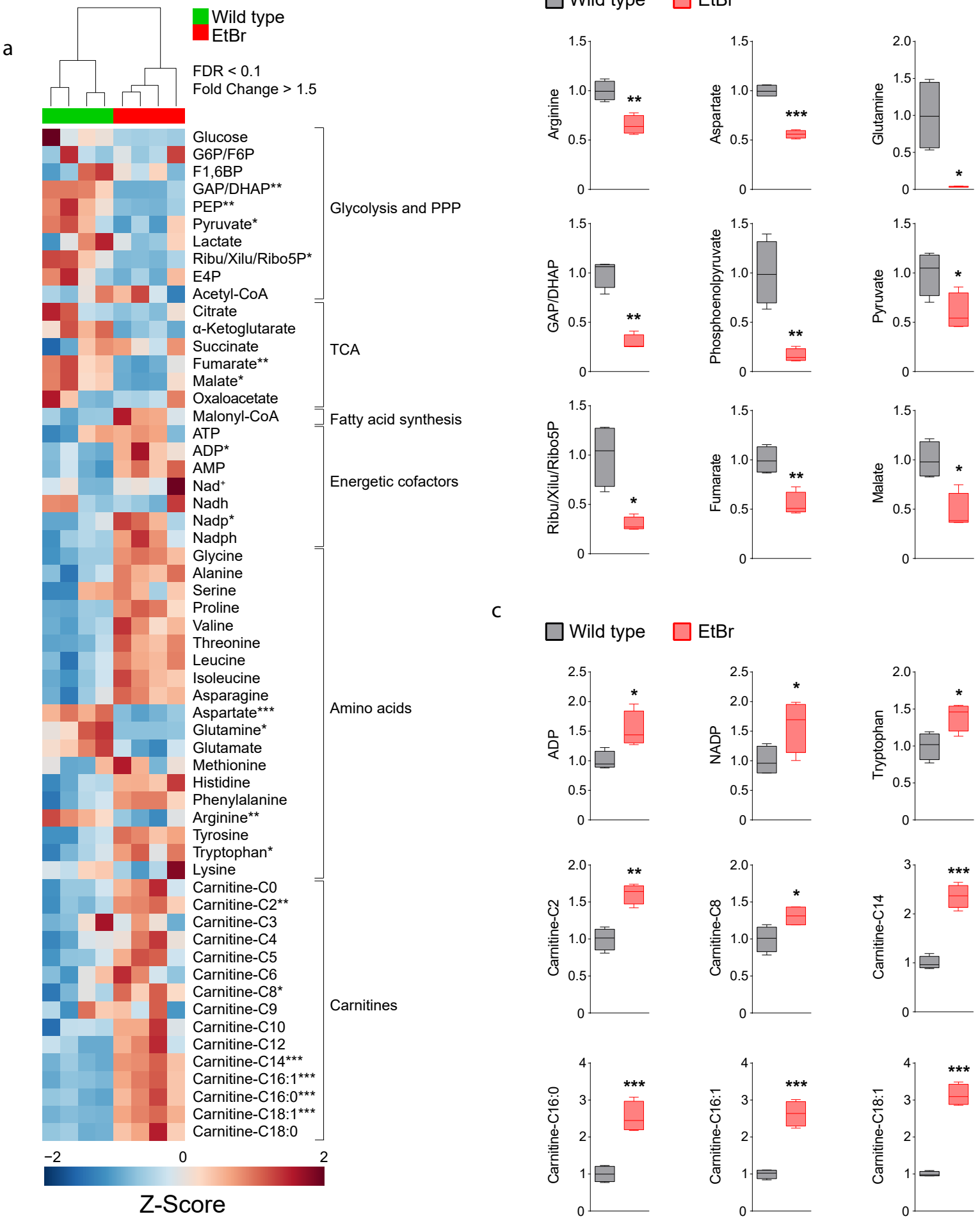
a
Wild type
EtBr
FDR < 0.1
Fold Change > 1.5
Glucose
G6P/F6P
F1,6BP
GAP/DHAP**
PEP**
Pyruvate*
Lactate
Ribu/Xilu/Ribo5P*
E4P
Acetyl-CoA
Citrate
α-Ketoglutarate
Succinate
Fumarate**
Malate*
Oxaloacetate
Malonyl-CoA
ATP
ADP*
AMP
Nad+
Nadh
Nadp*
Nadph
Glycine
Alanine
Serine
Proline
Valine
Threonine
Leucine
Isoleucine
Asparagine
Aspartate***
Glutamine*
Glutamate
Methionine
Histidine
Phenylalanine
Arginine**
Tyrosine
Tryptophan*
Lysine
Carnitine-C0
Carnitine-C2**
Carnitine-C3
Carnitine-C4
Carnitine-C5
Carnitine-C6
Carnitine-C8*
Carnitine-C9
Carnitine-C10
Carnitine-C12
Carnitine-C14***
Carnitine-C16:1***
Carnitine-C16:0***
Carnitine-C18:1***
Carnitine-C18:0
Glycolysis and PPP
TCA
Fatty acid synthesis
Energetic cofactors
Amino acids
Carnitines
−2
0
2
Z-Score
b
Wild type
EtBr
Arginine
Aspartate
Glutamine
GAP/DHAP
Phosphoenolpyruvate
Pyruvate
Ribu/Xilu/Ribo5P
Fumarate
Malate
c
Wild type
EtBr
ADP
NADP
Tryptophan
Carnitine-C2
Carnitine-C8
Carnitine-C14
Carnitine-C16:0
Carnitine-C16:1
Carnitine-C18:1

Figure 4

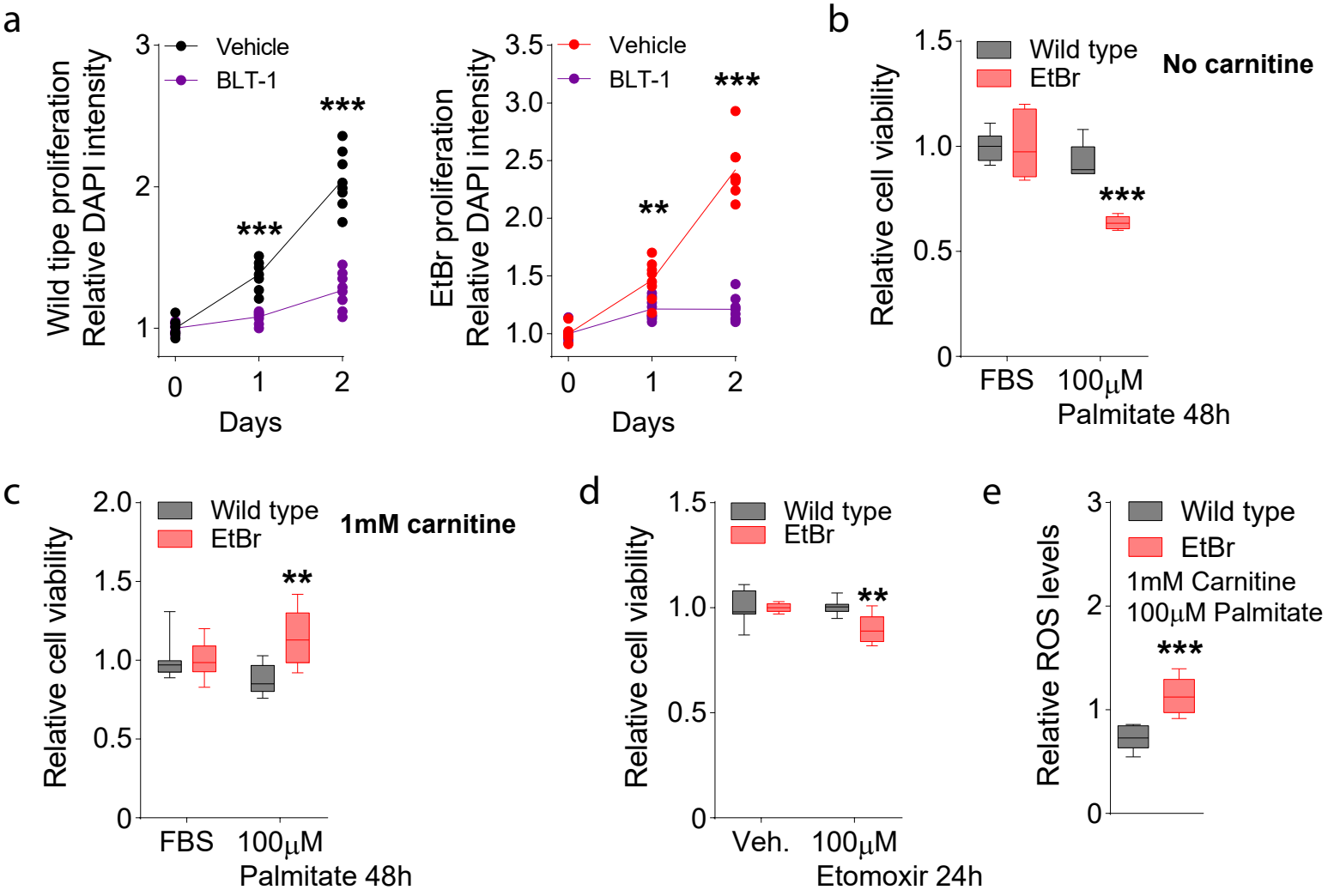
a
Wild tipe proliferation
Relative DAPI intensity
Vehicle
BLT-1
***
***
Days
EtBr proliferation
Relative DAPI intensity
Vehicle
BLT-1
**
***
Days
b
Relative cell viability
Wild type
EtBr
No carnitine
***
FBS
100μM
Palmitate 48h
c
Relative cell viability
Wild type
EtBr
1mM carnitine
**
FBS
100μM
Palmitate 48h
d
Relative cell viability
Wild type
EtBr
**
Veh.
100μM
Etomoxir 24h
e
Relative ROS levels
Wild type
EtBr
1mM Carnitine
100μM Palmitate
***

Figure 5

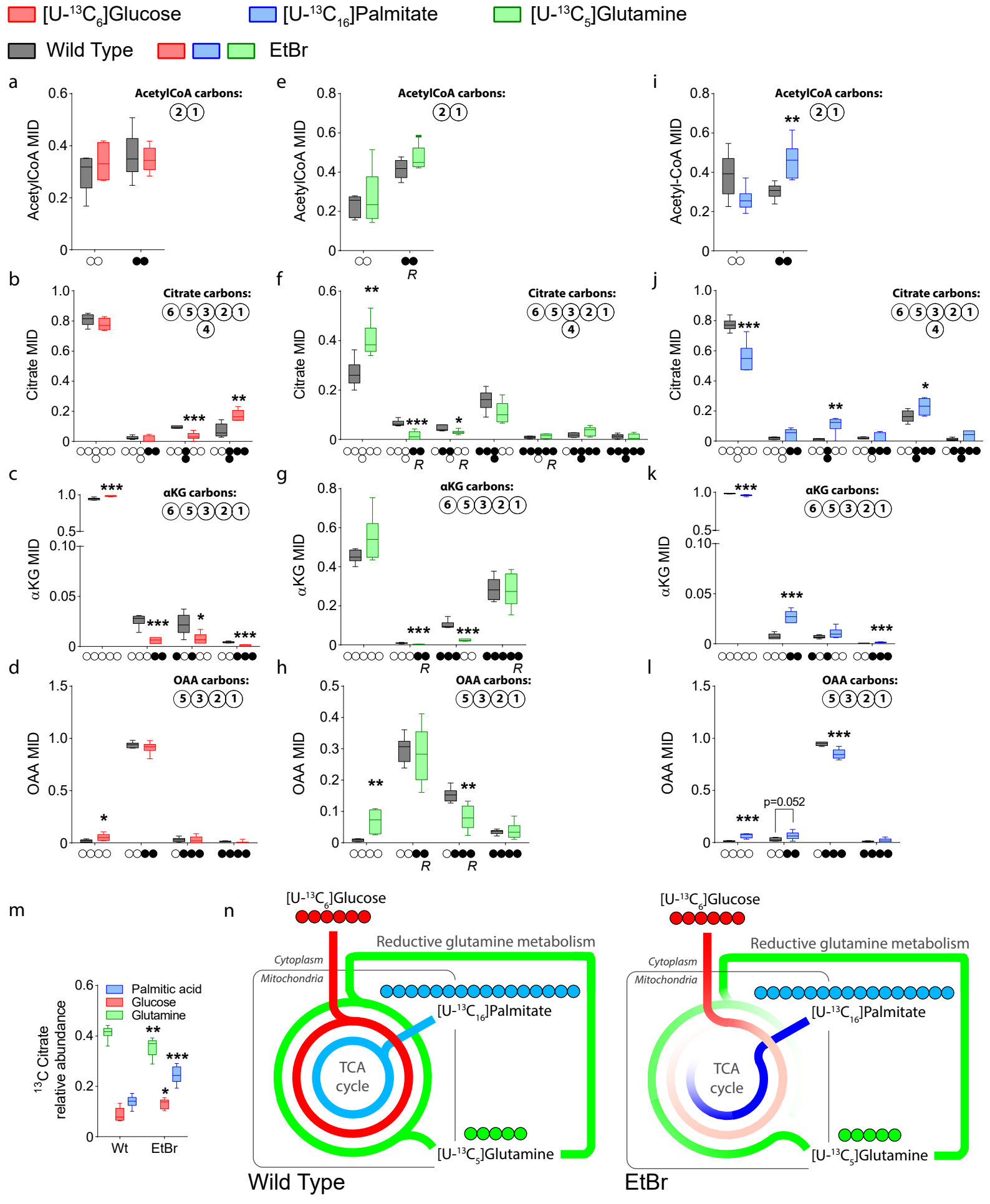
[U-13C6]Glucose
[U-13C16]Palmitate
[U-13C5]Glutamine
Wild Type
EtBr
a
AcetylCoA carbons:
AcetylCoA MID
e
AcetylCoA carbons:
AcetylCoA MID
i
AcetylCoA carbons:
Acetyl-CoA MID
b
Citrate carbons:
Citrate MID
f
Citrate carbons:
Citrate MID
j
Citrate carbons:
Citrate MID
c
αKG carbons:
αKG MID
g
αKG carbons:
αKG MID
k
αKG carbons:
αKG MID
d
OAA carbons:
OAA MID
h
OAA carbons:
OAA MID
l
OAA carbons:
OAA MID
p=0.052
m
Palmitic acid
Glucose
Glutamine
13C Citrate relative abundance
Wt
EtBr
n
[U-13C6]Glucose
Reductive glutamine metabolism
Cytoplasm
Mitochondria
[U-13C16]Palmitate
TCA cycle
[U-13C5]Glutamine
Wild Type
[U-13C6]Glucose
Reductive glutamine metabolism
Cytoplasm
Mitochondria
[U-13C16]Palmitate
TCA cycle
[U-13C5]Glutamine
EtBr

Figure 6

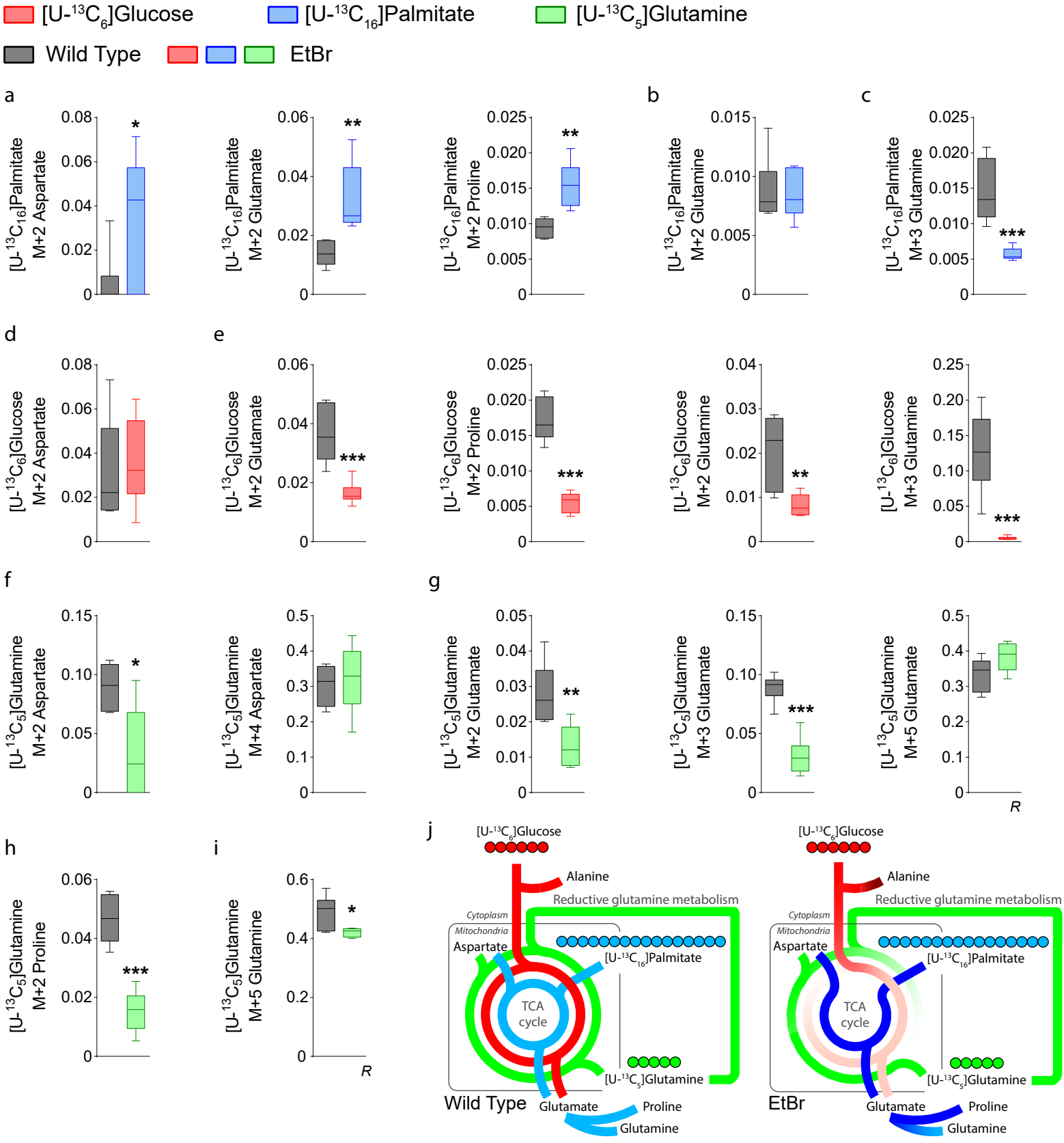
[U-13C6]Glucose
[U-13C16]Palmitate
[U-13C5]Glutamine
Wild Type
EtBr
a
[U-13C16]Palmitate M+2 Aspartate
[U-13C16]Palmitate M+2 Glutamate
[U-13C16]Palmitate M+2 Proline
b
[U-13C16]Palmitate M+2 Glutamine
c
[U-13C16]Palmitate M+3 Glutamine
d
[U-13C6]Glucose M+2 Aspartate
e
[U-13C6]Glucose M+2 Glutamate
[U-13C6]Glucose M+2 Proline
[U-13C6]Glucose M+2 Glutamine
[U-13C6]Glucose M+3 Glutamine
f
[U-13C5]Glutamine M+2 Aspartate
[U-13C5]Glutamine M+4 Aspartate
g
[U-13C5]Glutamine M+2 Glutamate
[U-13C5]Glutamine M+3 Glutamate
[U-13C5]Glutamine M+5 Glutamate
R
h
[U-13C5]Glutamine M+2 Proline
i
[U-13C5]Glutamine M+5 Glutamine
R
j
[U-13C6]Glucose
Alanine
Reductive glutamine metabolism
Cytoplasm
Mitochondria
Aspartate
[U-13C16]Palmitate
TCA cycle
[U-13C5]Glutamine
Wild Type
Glutamate
Proline
Glutamine
EtBr

Figure 7

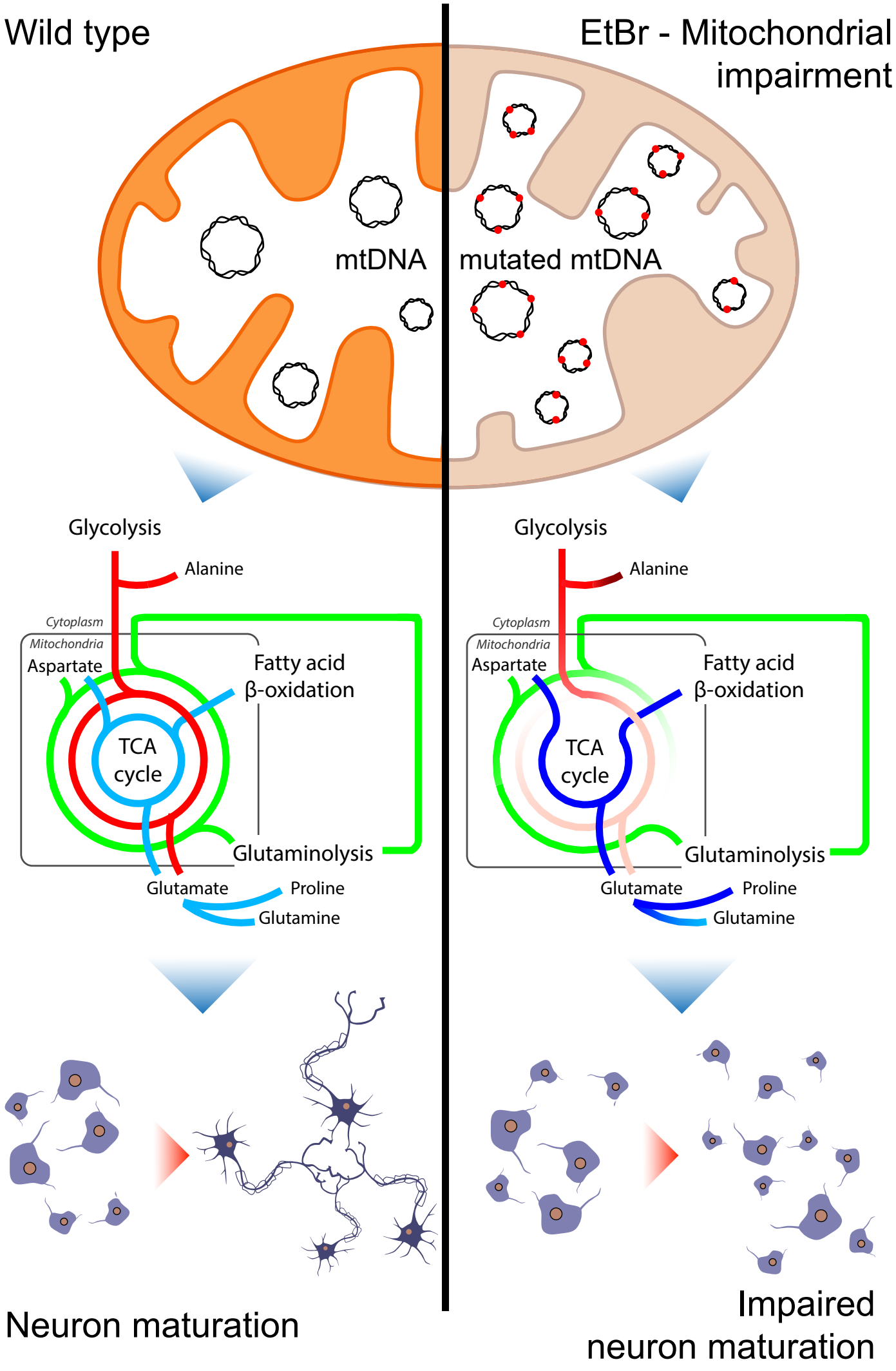
Wild type
EtBr - Mitochondrial impairment
mtDNA
mutated mtDNA
Glycolysis
Alanine
Cytoplasm
Mitochondria
Aspartate
Fatty acid β-oxidation
TCA cycle
Glutaminolysis
Glutamate
Proline
Glutamine
Glycolysis
Alanine
Cytoplasm
Mitochondria
Aspartate
Fatty acid β-oxidation
TCA cycle
Glutaminolysis
Glutamate
Proline
Glutamine
Neuron maturation
Impaired neuron maturation

Supplementary Figure 1

a

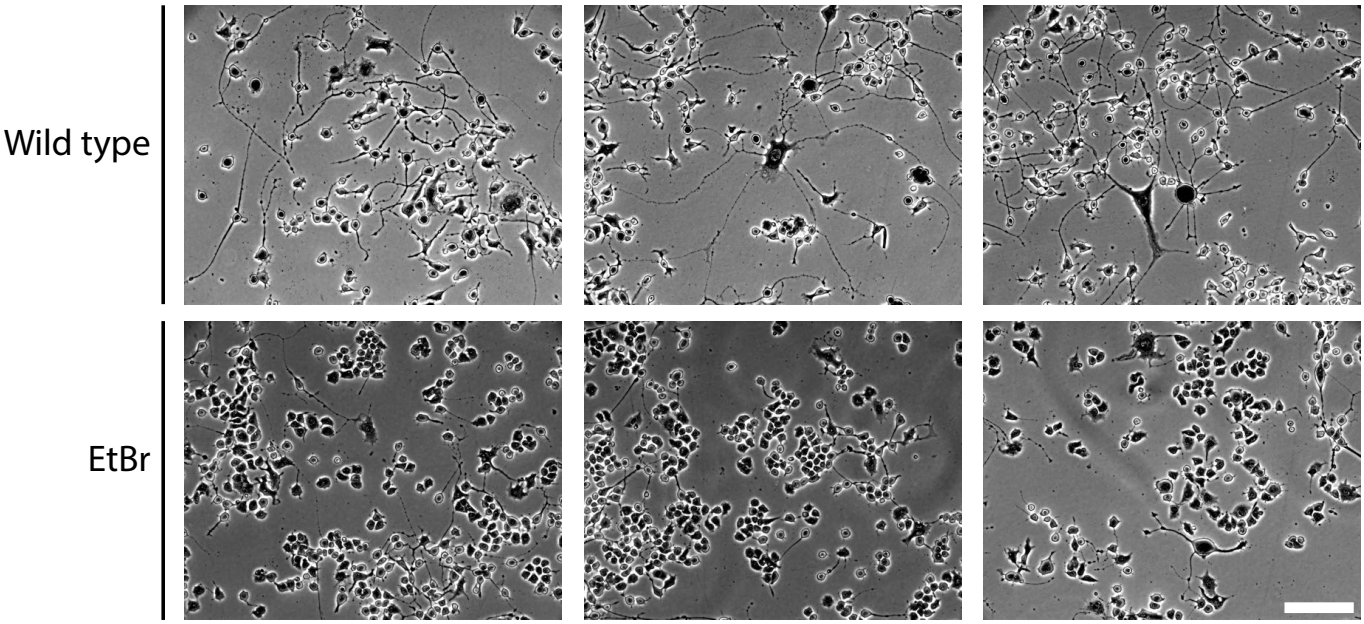

b

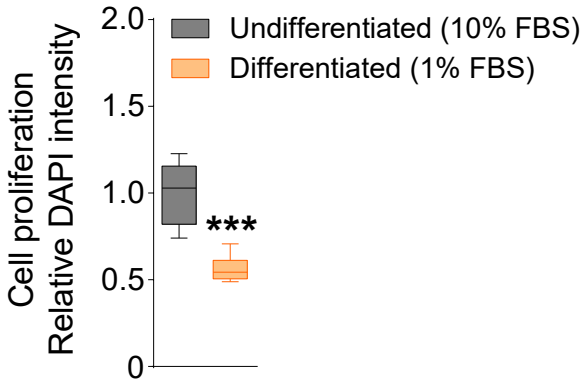

Supplementary Figure 2

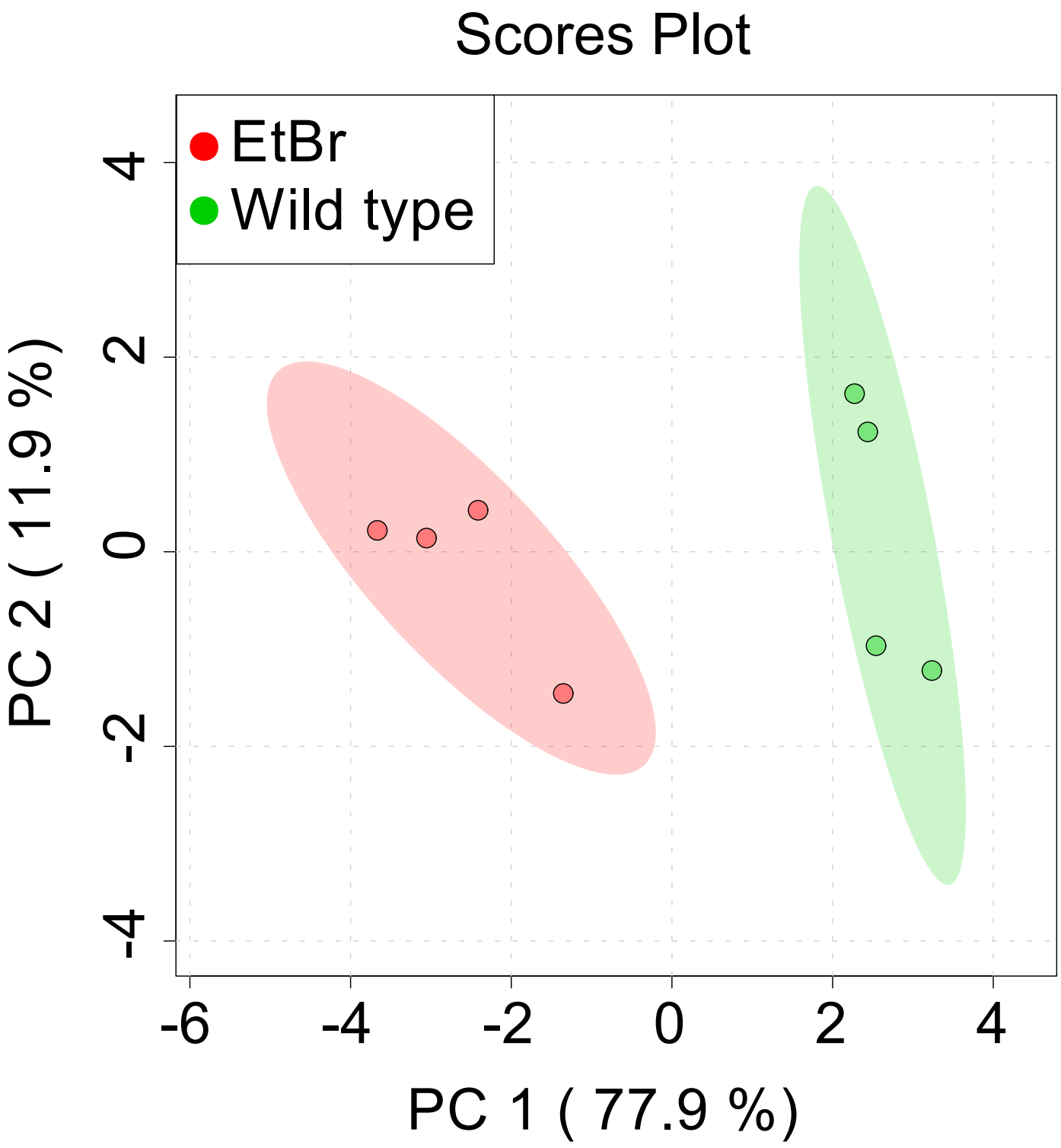

Supplementary Figure 3

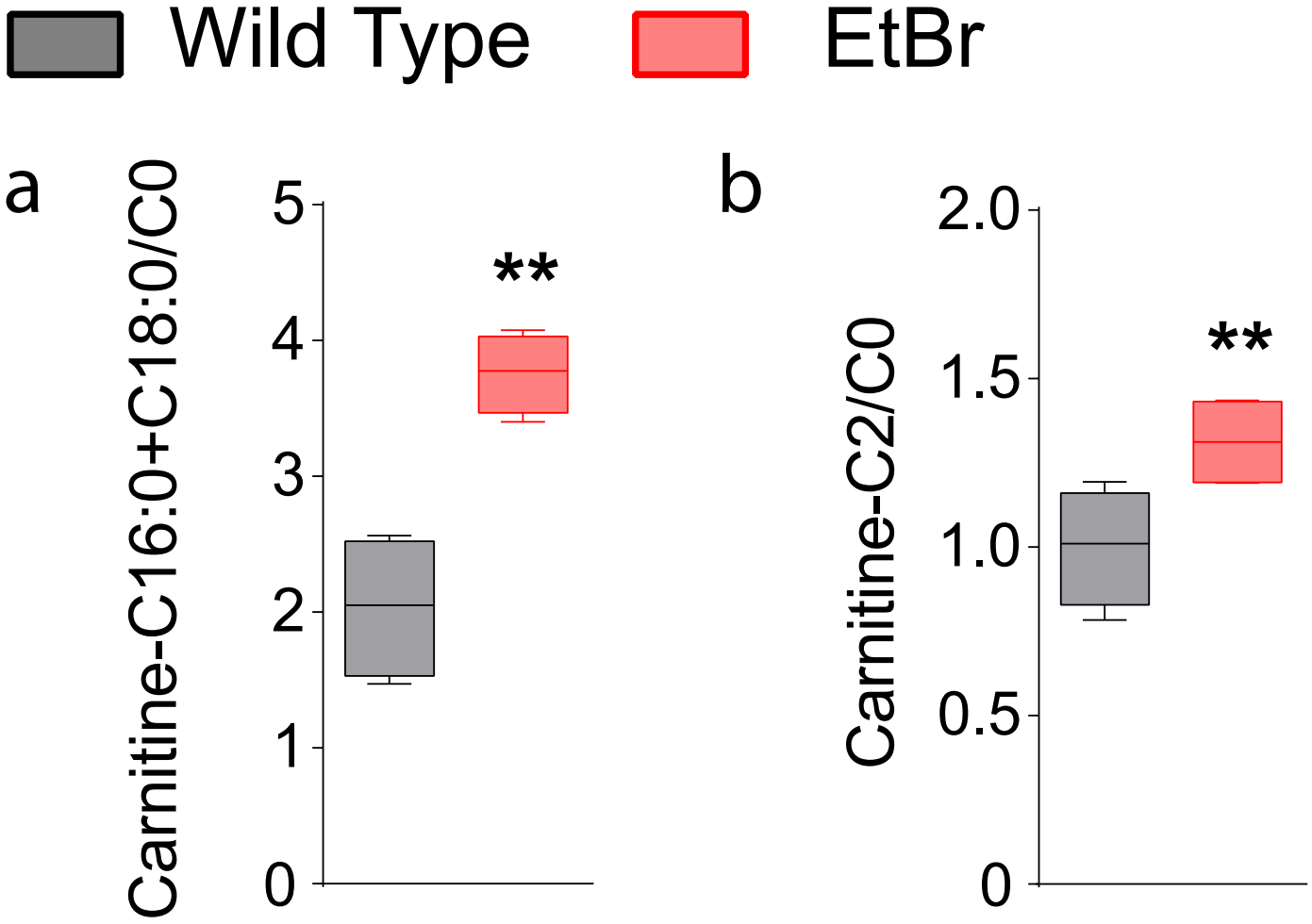

Supplementary Figure 4

a

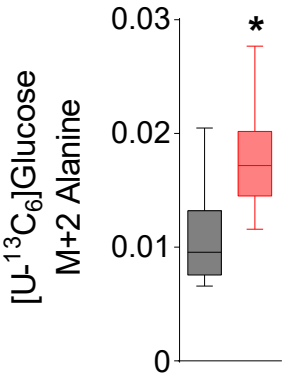

b

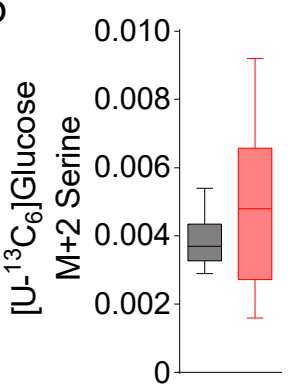

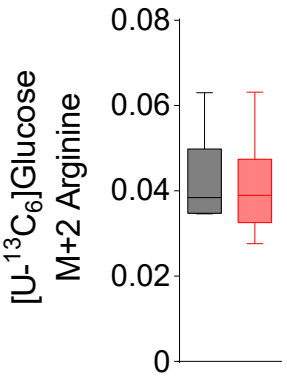

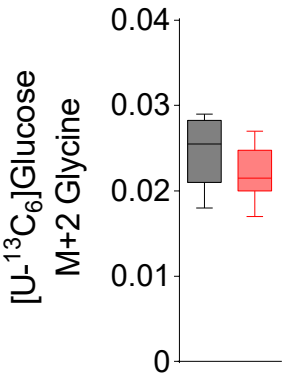

c

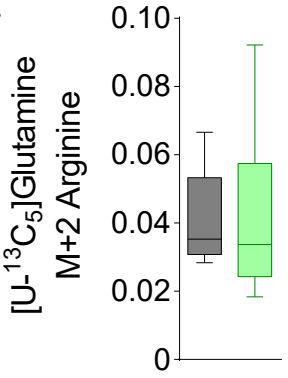

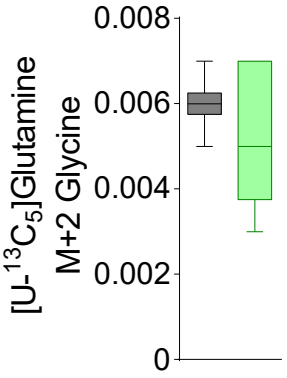

d